Geophysical Journal International

Geophys. J. Int. (2023) **233,** 663–679
Advance Access publication 2022 December 01
GJI Seismology

https://doi.org/10.1093/gji/ggac474

Normal mode observability of radial anisotropy in the Earth's mantle

F. Restelli [1], P. Koelemeijer [1,2] and A. M. G. Ferreira[3]

[1] *Department of Earth Sciences, Royal Holloway University of London, Egham TW20 0EQ, United Kingdom. E-mail: federica.restelli.2019@live.rhul.ac.uk (FR); paula.koelemeijer@earth.ox.ac.uk (PK)*
[2] *Department of Earth Sciences, University of Oxford, Oxford OX1 3AN, United Kingdom*
[3] *Department of Earth Sciences, University College London, London WC1E 6BT, United Kingdom*

Accepted 2022 November 25. Received 2022 November 18; in original form 2022 February 22

SUMMARY

Observations of seismic anisotropy provide useful information to infer directions of mantle flow. However, existing global anisotropic tomography models are not consistent, particularly in the lower mantle. Therefore, the interpretation of seismic anisotropy in terms of mantle dynamics and evolution remains difficult. While surface and body waves are commonly used to build radially anisotropic tomography models, they provide heterogeneous data coverage and the radial anisotropy structure retrieved using these data may be biased by the use of imperfect crustal corrections. Normal modes, the free oscillations of the Earth, automatically provide global data coverage and their sensitivity to shear wave (v_s) and compressional wave (v_p) velocity makes them suitable to study both v_s and v_p anisotropy in the mantle. In this study, we assess whether current normal mode splitting data have sufficient sensitivity to lower mantle anisotropy to potentially constrain it. We consider the uncertainties in the data and the effect of inaccuracies in crustal thickness corrections and the assumed scaling between v_p and v_s. We perform forward modelling of normal mode data using six different 3-D global radially anisotropic tomography models to document how strong and widespread anisotropy has to be to be observable in current normal mode data. We find that, on average 50% of the spheroidal and 55% of the toroidal modes investigated show significant sensitivity to v_s anisotropy, while roughly 57% of the spheroidal modes also have strong sensitivity to v_p anisotropy. Moreover, we find that the normal mode data fit varies substantially for the various anisotropic tomography models considered, with the addition of anisotropy not always improving the data fit. While we find that crustal thickness corrections do not strongly impact modes that are sensitive to the lower mantle, we observe a trade-off between radial anisotropy and v_p scaling for these modes. As long as this is taken into consideration, our findings suggest that existing normal mode data sets can provide valuable information on both v_s and v_p anisotropy in the mantle.

Key words: Composition and structure of the mantle; Tomography; Seismic anisotropy; Surface waves and free oscillations; Theoretical seismology.

1 INTRODUCTION

Seismic anisotropy, the dependence of seismic wave speed on direction, provides insights into mantle flow and thus dynamic processes in the mantle. Seismic anisotropy may be due to the alignment of intrinsically anisotropic minerals, such as olivine, following large-strain deformation due to mantle flow (LPO or lattice preferred orientation, e.g. Mainprice 2010), or from the alignment of structural elements, such as pockets of melt, cracks or fine layering (SPO or shape preferred orientation, e.g. Backus 1962; Kendall & Silver 1996).

To describe the most general case of anisotropy, 21 independent coefficients of the elastic tensor have to be defined (e.g. Montagner & Nataf 1986). Radial anisotropy, where the medium is considered to have hexagonal symmetry with a vertical symmetry axis, is the simplest type of anisotropy, which has been extensively investigated (e.g. Babuska & Cara 1991; Panning & Romanowicz 2006; Kustowski *et al.* 2008; Wang *et al.* 2013). Such a medium is completely described by 5 parameters—A, C, F, L and N, called Love coefficients (Love 1927). v_{sh}, v_{sv}, v_{ph} and v_{pv}—related to N, L, A and C, respectively—represent the velocity of the shear (v_s) and compressional (v_p) waves, with the subscripts 'h' and 'v' denoting horizontally and vertically polarized waves. The fifth parameter η (related to A, F and L) characterizes the dependence on the incident angle. Anisotropy in shear and compressional wave velocities is defined by $\xi = (v_{sh}/v_{sv})^2$ and $\phi = (v_{pv}/v_{ph})^2$, respectively. Robust

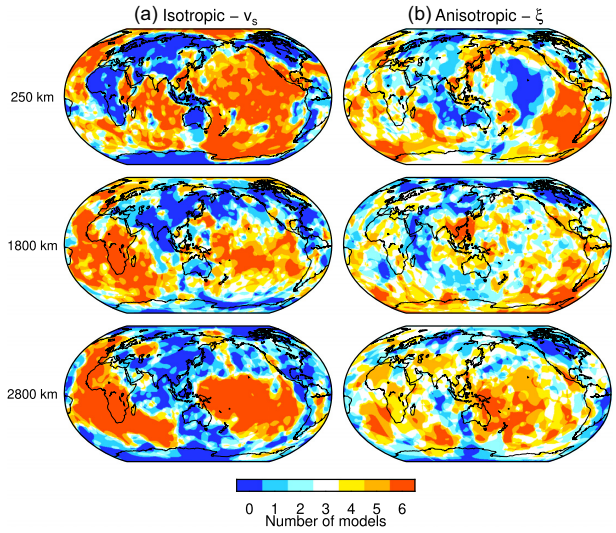

Figure 1. Vote maps of (a) negative shear wave velocities (v_s) and (b) radial v_s anisotropy (ξ) smaller than 1 at different depths in the mantle, incorporating six existing tomography models: SAW642ANb (Panning *et al.* 2010), savani (Auer *et al.* 2014), SEMUCB-WM1 (French & Romanowicz 2014), S362WMANI+M (Moulik & Ekström 2014), SGLOBE-rani (Chang *et al.* 2015) and SPani (Tesoniero *et al.* 2015). Dark red and blue colours imply agreement between models, while lighter colours indicate disagreement. Red colours in (a) indicate agreement on low v_s velocities, whereas red colours in (b) imply agreement on $\xi < 1$, that is v_{sv} larger than v_{sh}. Vote maps were constructed following the methodology by Shephard *et al.* (2017).

constraints on radial anisotropy thus potentially help to distinguish between horizontal and vertical mantle flow (e.g. Montagner 2002; Long & Becker 2010; Schaefer *et al.* 2011; Chang *et al.* 2016).

In the upper mantle, radial anisotropy is needed to explain the dispersion properties of both Rayleigh and Love waves simultaneously (e.g. Anderson 1961), leading to the inclusion of radial anisotropy in the Preliminary Reference Earth Model (PREM; Dziewonski & Anderson 1981). At these depths, radial anisotropy has also been observed consistently in different studies, finding for example radial anisotropy in v_s greater than 1 (fast v_{sh}) beneath the central Pacific at 250 km depth (e.g. Montagner & Tanimoto 1991; Auer *et al.* 2014) and $\xi < 1$ (fast v_{sv}) beneath the East Pacific Rise (e.g. Gu *et al.* 2005; Moulik & Ekström 2014).

While the bulk of the lower mantle is generally considered to be isotropic (Meade *et al.* 1995), the presence of seismic anisotropy has been invoked at the top as well as at the base of the lower mantle, both in regional studies of shear wave splitting (e.g. Lay & Helmberger 1983; Kendall & Silver 1996; Walpole *et al.* 2017) and in global tomography models that have been developed over the last decades (e.g. Panning & Romanowicz 2006; Kustowski *et al.* 2008; French & Romanowicz 2014; Auer *et al.* 2014; Moulik & Ekström 2014; Tesoniero *et al.* 2015; Chang *et al.* 2015). For more details about seismic anisotropy in the lower mantle inferred from seismological observations, and its connection to mantle dynamics, we refer the reader to comprehensive reviews of, for example Nowacki *et al.* (2011), Romanowicz & Wenk (2017) and Nowacki & Cottaar (2021).

Unlike global isotropic models, that nowadays show a large consistency between the imaged seismic anomalies throughout most of the mantle (Fig. 1a), global anisotropic models show substantial differences, even on the largest scales (Fig. 1b; e.g. Chang *et al.* 2014). Discrepancies between models are likely due to the fact that models employ different data types, model parametrizations, inversion techniques and theoretical approximations. A particular issue that arises in attempts to map anisotropy globally in the lowermost mantle is that the isotropic velocity structure leaks into the anisotropic structure retrieved in tomographic inversions (e.g. Kustowski *et al.* 2008; Chang *et al.* 2015). This is mainly due to an imbalance between v_{sv}- and v_{sh}-sensitive data used for probing the lowermost mantle in global anisotropic tomography inversions. Complementary data such as normal mode measurements are needed to address this issue, as discussed further below. Moreover, it has been demonstrated that inversions for deep anisotropic mantle structure are severely influenced by the crustal model used for crustal corrections of body wave and surface wave data (e.g. Ferreira *et al.* 2010; Panning *et al.* 2010; Chang & Ferreira 2017). Consequently, the presence of large-scale anisotropy in the deep mantle remains debated at present-day.

Besides body waves and surface waves, which are most commonly employed in studies of seismic anisotropy, normal modes (Earth's free oscillations) are also sensitive to the anisotropic structure of the mantle (e.g. Dahlen & Tromp 1998). The advantage of using normal modes in global tomography is that they automatically provide global data coverage and are directly sensitive to both v_s and v_p anisotropy, removing the need of scaling relationships to describe v_p structure. Normal mode splitting measurements were included by Moulik & Ekström (2014) and Moulik & Ekström (2016) to constrain radial v_s anisotropy in the mantle, which decreased trade-offs between isotropic velocity and anisotropy. These studies did not include observations of core–mantle boundary (CMB) Stoneley modes (Koelemeijer *et al.* 2013), that are highly sensitive to structures in the lowermost mantle, nor the recent toroidal mode measurements reported by Schneider & Deuss (2021). At the same time, these older studies focused on v_s anisotropy without considering anisotropy in v_p. Furthermore, normal mode measurements were combined with other observations in joint inversions, making it not straightforward to unravel their specific ability to constrain radial anisotropy. Finally, while the effect of crustal corrections on body wave traveltimes (Ritsema *et al.* 2009), body wave waveforms (Marone & Romanowicz 2007; Panning *et al.* 2010) and surface waves (Ferreira *et al.* 2010) has been investigated, it is not clear to what extent normal mode models are affected by the use of different crustal corrections.

The aim of this study is to investigate the ability of normal modes to observe both v_s and v_p anisotropy in the Earth's mantle and to assess the additional insights they may bring to tomographic inversions. Rather than basing our investigations on theoretical sensitivity kernels, we make use of the data uncertainties of existing normal mode observations to study what current normal-mode data may be able to resolve, akin Koelemeijer *et al.* (2012). We expand on their investigations of radial anisotropy by using realistic anisotropy structures as imaged by global tomography. Given the variability in seismic anisotropy in such models, we base our study on six existing tomography models, which display differences in seismic anisotropy both in terms of amplitudes and wavelengths. Using forward modelling, we compare model predictions to both data uncertainties and the actual observations, as well as to the effect of different crustal thickness corrections.

This manuscript is structured as follows. Section 2 briefly summarizes important aspects of normal mode theory relevant to this study. In Section 3, we discuss the details of the data sets considered, the input models used as well as the way we compute crustal corrections and the concept of observability. Throughout Section 4 we use observability to investigate how strong and widespread anisotropy should be to be observed by current normal mode data. These

investigations allow us to identify which normal modes are particularly useful for detecting seismic anisotropy in specific regions of the mantle. Section 5 details the trade-offs that may exist between radial anisotropy and other parameters, such as crustal thickness and the scaling between v_s and v_p. In Section 6, we compute the misfit between observed and predicted splitting functions for the different tomography models used in the forward modelling, both with and without lateral variations in anisotropy. This way, we examine the effect of anisotropic versus isotropic structure on normal mode data fit, and we quantify how well existing global tomography models fit current normal mode observations. Finally, in Section 7 we discuss some limitations of our approach as well as implications and guidance for future inversions of normal mode data for 3-D global radial anisotropy.

2 NORMAL MODE THEORY

Free oscillations or normal modes of the Earth arise after large earthquakes (typically with moment magnitude $M_w > 7.4$) when the Earth resonates like a bell. Due to the finite size of the Earth, only discrete resonance frequencies are permitted. Two different types of normal modes exist: (i) spheroidal modes, which involve vertical and horizontal motion, and (ii) toroidal modes, which involve horizontal motions only. Spheroidal mode multiplets ${}_nS_l$ and toroidal mode multiplets ${}_nT_l$ are characterized by their radial order n and angular order l. Each multiplet consists of $2l + 1$ singlets with azimuthal order m. For a spherically symmetric, non-rotating, perfectly elastic and isotropic (SNREI) Earth model, all $2l + 1$ singlets of a given mode are degenerate, that is have the same frequency. Earth's rotation, ellipticity and aspherical structure—including topography on internal boundaries and lateral variations in isotropic and anisotropic structure—remove this degeneracy, resulting in so-called splitting of the multiplet. In the real Earth, normal modes may exchange energy ('coupling'), but in this study we only consider multiplets in isolation ('self-coupling') though some of the observed self-coupled splitting functions were obtained using pair or group-coupling. The self-coupling approximation is commonly used in tomographic applications, but does limit us to study even-degree heterogeneity only.

The splitting of a given mode is conveniently described by splitting function coefficients, introduced by Woodhouse *et al.* (1986). Using perturbation theory, these coefficients, denoted as c_{st}, are linearly related to the perturbations of the reference Earth model as follows:

$$c_{st} = \int_0^a \delta m_{st}(r) K_s(r) \mathrm{d}r + \sum_d \delta h_{st}^d H_s^d \qquad (1)$$

where s and t are the angular order s and azimuthal order t describing lateral heterogeneity in the Earth. In the isotropic case, δm_{st} are the coefficients for perturbations in shear wave velocity (v_s), compressional wave velocity (v_p) and density (ρ). In the anisotropic case, δm_{st} include perturbations in v_{sh}, v_{sv}, v_{ph}, v_{pv} and ρ. δh_{st} refer to perturbations in topography at internal boundaries. $K_s(r)$ and H_s^d are the sensitivity kernels associated with the perturbations, computed in this study for the anisotropic PREM model (Dziewonski & Anderson 1981).

Splitting function coefficients can be visualized using splitting function maps $c(\theta, \phi)$:

$$c(\theta, \phi) = \sum_{s=0}^{2l} \sum_{t=-s}^{s} c_{st} Y_s^t(\theta, \phi) \qquad (2)$$

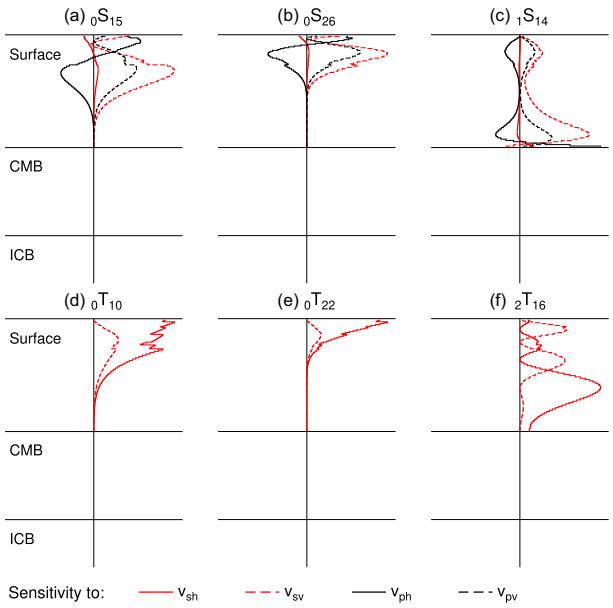

Figure 2. Example sensitivity kernels of spheroidal and toroidal modes for mantle structure at degree $s = 2$. We show the sensitivity to horizontally and vertically polarized shear wave velocity (bold and dashed red lines, respectively) and horizontally and vertically polarized compressional wave velocity (bold and dashed black lines, respectively), calculated for the anisotropic PREM model. Horizontal lines indicate the surface and the radii of the core-mantle boundary (CMB) and inner core boundary (ICB). Each panel is normalized independently. Kernels for other spherical harmonic degrees are presented in Fig. S1.

where Y_s^t are the complex spherical harmonics of Edmonds (1960). At a given latitude θ and longitude ϕ, the splitting function can be interpreted as the local, depth-weighted frequency relative to the degenerate frequency of the multiplet.

Fig. 2 shows examples of anisotropic sensitivity kernels $K_s(r)$ at degree ($s = 2$) for a few relevant spheroidal and toroidal normal modes. As expected, spheroidal modes show more sensitivity to v_{sv} than v_{sh}. For fundamental modes, the sensitivity to v_{sv} becomes progressively shallower for higher l (Figs 2a and b). Some modes of the first overtone branch ($n = 1$, $11 \leq l \leq 14$) are sensitive to v_{sv} in D″ (Fig. 2c). This CMB Stoneley mode behaviour continues into the second overtone branch until $l = 24$ and then the sensitivity to D″ shifts to the third overtone branch. Fundamental toroidal modes are mainly sensitive to v_{sh} in the upper mantle, and, as for spheroidal modes, their sensitivity becomes shallower for higher l (Figs 2d and e). The recent measurements of toroidal mode overtones (Schneider & Deuss 2021) provide improved sensitivity to v_{sh} in the lower mantle (e.g. Fig. 2f). A comparison between sensitivity kernels for degree 0, 2 and 4 is shown in Fig. S1.

3 DATA AND METHODOLOGY

3.1 Normal mode observations

Splitting function measurements are generally obtained from the non-linear, iterative, least-square inversion (Tarantola 1987) of seismic spectra (e.g. Resovsky & Ritzwoller 1998; Deuss *et al.* 2013) or alternatively using autoregressive estimation (Masters *et al.* 2000). Here, we use measurements with corresponding uncertainties from Masters *et al.* (2000), Deuss *et al.* (2013), Koelemeijer *et al.* (2013) and Koelemeijer (2014) for spheroidal modes, while for toroidal

modes we use observations from Resovsky & Ritzwoller (1998) and Schneider & Deuss (2021). In the case of duplicate measurements, we only use the most recent observations. To determine data uncertainties, most of these studies use a bootstrap resampling technique to remeasure splitting coefficients, making sure to leave out entire events in each inversion. Since we are primarily interested in mantle anisotropy, we do not use inner core-sensitive modes, resulting in a data set of 149 spheroidal modes and 52 toroidal modes (see Table S1 for a complete overview).

3.2 Mantle models

For our analysis we use six radially anisotropic tomography models from the literature: (i) SAW642ANb (Panning *et al.* 2010), (ii) savani (Auer *et al.* 2014), (iii) SEMUCB-WM1 (French & Romanowicz 2014), (iv) S362WMANI+M (Moulik & Ekström 2014), (v) SGLOBE-rani (Chang *et al.* 2015) and (vi) SPani (Tesoniero *et al.* 2015). While the first five models only describe variations in shear wave anisotropy, the latter also includes compressional wave anisotropy. Most of these models combine observations of body waves (traveltimes and/or waveforms) and surface waves (mostly phase velocities), with the exception of S362WMANI+M that also includes normal mode splitting function measurements (albeit only up to 3 mHz). For all models, we use the same $v_p - v_s$ and $\rho - v_s$ scaling relationships as used in the construction of the models (i.e. scaling factors of 0.5 or 0.55 for $v_p - v_s$ and 0.3 - 0.4 for $\rho - v_s$, depending on the model).

Given our focus on the sensitivity of normal modes to both v_s and v_p anisotropy, we are interested in variations in both ξ and ϕ, which only model SPani provides. For SAW642ANb and SEMUCB-WM1, we calculate ϕ consistently with how the models were constructed, that is using $d\ln\phi = -1.5 \times d\ln\xi$ (Panning & Romanowicz 2006). For S362WMANI+M, savani and SGLOBE-rani, we scale variations in v_{pv} and v_{ph} accordingly to v_{sv} and v_{sh}, using the same $v_p - v_s$ scaling relations as used in the construction of the isotropic parts of the models, as specified above.

Not all models use the 1-D model PREM as reference model (e.g. S362WMANI+M describes variations relative to model STW105 (Kustowski *et al.* 2008)). To ensure all variations are with respect to the same reference model and thus consistent with the normal mode kernels, we compute (where necessary) the absolute velocities in each model and then recalculate velocity perturbations with respect to PREM. For all models, we keep η the same as in PREM.

We summarize some characteristics of the (an)isotropic shear wave velocity structure of these tomographic input models in Figs 1 and 3. As discussed before, isotropic shear wave velocities are consistent across all models, but the overall agreement on the anisotropic parts of the models is poor (Fig. 1). Some common features can still be identified. For example, radial anisotropy greater than 1 ($\xi > 1$) is found beneath the Central Pacific at shallow depths (~150 km, Fig. 3) in all models. Radial anisotropy smaller than 1 ($\xi < 1$) is associated with the Large-Low-Velocity-Provinces (LLVPs) in the lowermost mantle, which may however mostly be an artefact caused by the leakage of isotropic structure into anisotropic structure (e.g. Kustowski *et al.* 2008; Chang *et al.* 2014). $v_{sh} > v_{sv}$S is generally found in the regions that surround the LLSVPs in the bottom few hundred kilometres of the mantle, where isotropic shear wave velocities are higher than average (Romanowicz & Wenk 2017).

However, the discrepancies between the models are larger than these similarities. First of all, the amplitudes of anisotropy anomalies vary significantly between models, especially in the lower mantle (e.g. at 1800 km depth, Fig. 3), where the resolution and robustness of anisotropy anomalies are weak (e.g. Chang *et al.* 2014). This may be due to high damping values used in some models to moderate the trade-off between isotropic and anisotropic structure. The length scales of heterogeneity are also different, with SPani and SGLOBE-rani containing smaller wavelength features than models such as SEMUCB-WM1 and SAW642ANb. Moreover, the anisotropy patterns vary across models. For example, at the base of the mantle (~2800 km), fast v_{sh} anomalies are found under north-western Africa in model S362WMANI+M, while fast v_{sv} anomalies are observed in models SAW642ANb and SPani.

In all models, the radial average of radial anisotropy decreases in amplitude with depth until the D″ region (Fig. 4a). However, details vary with SAW642ANb showing the strongest anisotropy in the upper mantle and only models SEMUCB-WM1, SPani and S362WMANI+M displaying significant anisotropy in the D″ region. These differences in anisotropy patterns and amplitudes observed across the six tomography models allow us to test a wide range of realistic (constrained by observations) input structures for normal mode predictions. Moreover, the current limited constraints on global anisotropy in the lower mantle highlight that additional data such as normal mode measurements may enhance the quality of future global anisotropy models.

3.3 Crustal models

Accurate crustal corrections are needed to avoid mapping crustal features into mantle structure during tomographic inversions. Generally, crustal corrections involve corrections for variations in crustal velocities and topography on crustal interfaces. For normal modes, the effect of crustal velocities is typically neglected as the crust is only a fraction of the wavelength of the data. We have verified that the effect of crustal velocities on normal mode splitting functions is only <0.5% compared to the effect of variations in crustal topography, consistent with work by Moulik & Ekström (2014). Therefore, we also neglect variations in crustal velocities, with our crustal corrections thus made up of three different contributions, including a correction for surface topography, water depth and Moho depth. While surface topography and water depth can safely be assumed to be known, Moho depth variations (or crustal thickness variations when combined with surface topography) have larger uncertainties and are thus of primary interest here. Over the years, crustal thickness models have been developed using different methods and data. Some are *a priori* models based on compilations of seismic reflection data, geophysical modelling or tectonic features (e.g. Nataf & Ricard 1996; Mooney *et al.* 1998), while others are obtained from actual inversions of seismic data (e.g. Meier *et al.* 2007).

Here, we investigate the effect of crustal thickness variations on normal modes using five different crustal models: CRUST5.1 (Mooney *et al.* 1998), CRUST2.0 (Bassin *et al.* 2000), CRUST1.0 (Laske *et al.* 2013), CRUST-SG (Chang *et al.* 2015) and CRUST-SEM (French & Romanowicz 2014). CRUST5.1, CRUST2.0 and CRUST1.0 have all been developed using data from seismic refraction experiments, sediment thickness and receiver functions as well as gravity measurements, with updates in these data sets resulting in finer crustal thickness grids (from 5° spacing for CRUST5.1 to 2° for CRUST2.0 and 1° for CRUST1.0). On the other hand, CRUST-SG

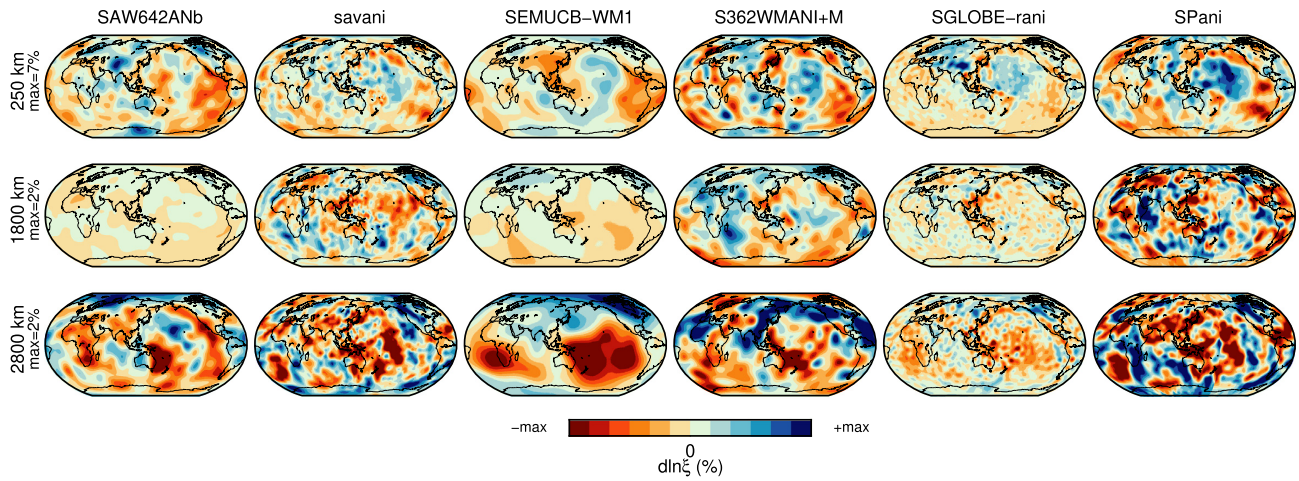

Figure 3. Comparison of lateral variations in radial anisotropy (dlnξ) across different tomography models, showing structure for (a) 250 km depth, (b) 1800 km depth and (c) 2800 km depth. Variations in ξ (v_s anisotropy) are plotted relative to anisotropic PREM ($\xi = 1$) for models SAW642ANb, savani, SEMUCB-WM1, S362WMANI+M, SGLOBE-rani and SPani. Negative variations thus imply $\xi < 1$ and positive variations represent $\xi > 1$. Note that the 1-D average of each model is subtracted at each depth.

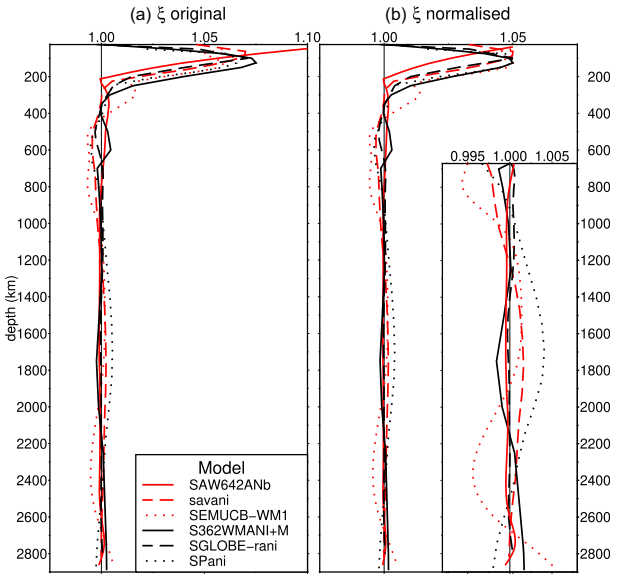

Figure 4. Radial average of ξ (representing v_s anisotropy) with depth for the six models used in this study, showing in (a) the amplitude of anisotropy in the original models, while in (b) the maximum radial value of ξ is normalized to 1.05. The insert magnifies how the amplitude of anisotropy changes below 670 km.

and CRUST-SEM were developed conjointly with mantle tomography models SGLOBE-rani (Chang *et al.* 2015) and SEMUCB-WM1 (French & Romanowicz 2014), respectively. In particular, Chang *et al.* (2015) first applied crustal corrections to all data using CRUST2.0, and then estimated crustal thickness perturbations in a joint inversion, primarily using short-period surface wave group velocity data. French & Romanowicz (2014) instead iteratively adjusted their crustal model using fundamental mode dispersion data, while fitting a large waveform data set in inversions for mantle structure. We note that in CRUST-SEM the Moho depth in the oceans is fixed at 30 km and thus is not realistic, with this model primarily representing an 'equivalent' crustal structure that fits the used data well.

3.4 Observability

We calculate synthetic splitting functions for the six mantle tomography models presented in Section 3.2 along with the associated crustal thickness model that was used in the construction of the mantle model, that is we use CRUST2.0 for SPani, savani, SAW642ANb and S362WMANI+M, CRUST-SG for SGLOBE-rani and CRUST-SEM for SEMUCB-WM1. Other contributions to the crustal corrections are given by the surface topography and water-land distribution, which we consider to be well-known and take from CRUST5.1. No corrections are made for Earth's rotation and ellipticity, as the observed splitting functions have already been corrected for those effects. These predicted splitting function coefficients are subsequently used to estimate the observability of v_s and v_p anisotropy in the mantle, as explained in more detail below.

The concept of observability was introduced by Koelemeijer *et al.* (2012) as a useful tool to determine whether the signal in synthetic data due to particular structures in the mantle is significant enough compared to the data uncertainties. We thus calculate observability for v_s and v_p radial anisotropy in the mantle for different spherical harmonic degrees s according to:

$$O_s^{\text{aniso}} = \frac{1}{2s+1} \sum_{t=-s}^{s} \frac{|c_{st}^{\text{aniso}} - c_{st}^{\text{iso}}|}{\sigma_{st}^{\text{data}}} \tag{3}$$

where s and t are the angular and azimuthal orders of the spherical harmonic expansion used to describe heterogeneity in the Earth, c_{st}^{aniso} and c_{st}^{iso} are the predicted splitting function coefficients for the full anisotropic model or just its isotropic part, respectively, and $\sigma_{st}^{\text{data}}$ are the associated uncertainties in the observed splitting function coefficients. If the effect of anisotropy is larger than the data uncertainties, that is $O_s^{\text{aniso}} > 1$, then we consider the anisotropy to be observable. On the contrary, when $O_s^{\text{aniso}} < 1$, the signal due to anisotropy is not large enough to be observed by current normal mode observations. The ability of normal modes to observe seismic anisotropy therefore depends on several factors: the strength of anisotropy in the models themselves, the uncertainties in the data as well as the theoretical sensitivity of normal modes, which may all vary for different spherical harmonic degrees.

Normal modes are sensitive to the entire mantle (and core), with the observed frequency representing a depth-weighted average due

to Earth structure at different depths. To understand which normal modes are particularly able to constrain radial anisotropy at specific depths, we also confine the anisotropy to certain depth ranges, using only the isotropic part of the input model in the rest of the mantle. Since the calculation of observability involves the difference between the anisotropic and isotropic input models, the isotropic perturbations cancel out at all depths and the observability we obtain is only due to anisotropy in the specified depth range.

As noted before (see also Figs 3 and 4), the amplitude of anisotropy varies between the different input models. In order to study the effect of lateral variation patterns in anisotropy alone on the observability, we scale the anisotropy of different models by setting the maximum radial average of anisotropy to 1.05 (i.e. the radial average of the anisotropy perturbations is 5%). We then recalculate absolute and relative variations in v_{sh} and v_{sv}, ensuring at the same time that the isotropic Voigt average velocities remain the same as in the original models (following Panning & Romanowicz (2006) for the case that $\eta \sim 1$). The resulting normalized models are again used to compute synthetic splitting functions. The radial average of ξ in both the original and normalized models is plotted with depth for each model in Fig. 4. While the radially averaged amplitude of anisotropy is very comparable across all the tomography models in the upper mantle, we do note that the amplitudes in the deepest mantle remain different (see insert in Fig. 4b).

The observability between two normalized anisotropy models informs us whether normal modes can distinguish between different patterns in anisotropy. A similar exercise was taken by Koelemeijer *et al.* (2012) for differences between CMB topography models. In this case, we adopt SGLOBE-rani as reference model and calculate the observability for lateral variations in anisotropy according to:

$$O_s^{\text{pattern}} = \frac{1}{2s+1} \sum_{t=-s}^{s} \frac{|(c_{st}^{\text{aniso}} - c_{st}^{\text{iso}})^{<m>} - (c_{st}^{\text{aniso}} - c_{st}^{\text{iso}})^{<SG>}|}{\sigma_{st}^{\text{data}}} \tag{4}$$

where superscripts $^{<SG>}$ and $^{<m>}$ denote respectively the splitting function coefficients for the normalized anisotropic model SGLOBE-rani and any of the other normalized anisotropy models (SAW642ANb, savani, SEMUCB-WM1, S362WMANI+M or SPani), as well as their isotropic parts. As the isotropic parts cancel out for both models, the observability only considers the effect of different patterns in anisotropy.

To study possible trade-offs between crustal thickness and anisotropy, we are interested to know whether normal modes are affected by the use of different crustal thickness models. To investigate this, we also use the concept of observability, comparing splitting function predictions for different crustal models relative to the reference crustal model:

$$O_s^{\text{crust}} = \frac{1}{2s+1} \sum_{t=-s}^{s} \frac{|c_{st}^{\text{crust}} - c_{st}^{\text{CRUST2.0}}|}{\sigma_{st}^{\text{data}}} \tag{5}$$

where $c_{st}^{\text{CRUST2.0}}$ denote the splitting function coefficients for the reference case of isotropic SGLOBE-rani with CRUST2.0 on top. c_{st}^{crust} are the splitting function predictions for isotropic SGLOBE-rani with either crustal model CRUST1.0, CRUST5.1, CRUST-SG or CRUST-SEM on top. Since the underlying mantle structure is kept the same, the observability only compares the effect of using a different crustal thickness model to the data uncertainties.

3.5 Misfit calculation

To investigate how well the tomographic models considered in this study fit currently available normal mode data, we calculate the L2 misfit between splitting function predictions and observations at degree s according to:

$$L_s^2 = \frac{1}{N} \sum_{N} \frac{1}{2s+1} \sum_{t=-s}^{s} \left| c_{st}^{\text{model}} - c_{st}^{\text{data}} \right|^2 \tag{6}$$

where N is the number of modes, c_{st}^{model} and c_{st}^{data} are the predicted and observed splitting function coefficients, respectively (Soldati *et al.* 2013). We choose not to normalize the misfit as otherwise small coefficients ($c_{st} \ll 1$) would dominate the misfit even though they contain little information about Earth structure.

For each tomography model, the misfit is calculated for predictions obtained using only the isotropic part of the model, as well as for predictions incorporating v_s anisotropy (and v_p anisotropy for SPani). For each model, we include corrections for crustal structure as described in Section 3.3. We evaluate the misfit both for structural degree 2 individually or all degrees together (up to $s_{\max} = 12$ for spheroidal modes and $s_{\max} = 6$ for toroidal modes). For the models with anisotropy included, we calculate the misfit taking into account all 149 normal modes in this study, or subsets of normal modes with specific sensitivity to specific depths, that is fundamental modes ($_0S_{20}$ to $_0S_{30}$) for the upper mantle and Stoneley modes ($_1S_{11}$ to $_1S_{14}$, $_2S_{15}$, $_2S_{16}$, $_2S_{17}$, $_2S_{25}$, $_3S_{26}$) for the lower mantle. For a few selected models, we also compute the misfit for different crustal thickness models or v_p scaling factors.

4 OBSERVABILITY OF MANTLE ANISOTROPY

In this section, we present the results for observability, discussing both v_s and v_p anisotropy as well as the observability of different crustal thickness models. In all cases, structure is considered to be observable in current normal mode data sets when the observability is greater than 1.

4.1 Anisotropy in the whole mantle

First of all, we present results for degree 2 ($s = 2$) structure only. Fig. 5 gives observability values as histograms for each tomographic model, showing both v_s and v_p anisotropy for spheroidal modes, while only v_s anisotropy results are given for toroidal modes.

For spheroidal modes, the models with the highest number of normal modes able to observe anisotropy are, in descending order, SEMUCB-WM1, S362WMANI+M, SPani and savani. In particular, for these models 50–80% of the modes have $O_2^{\text{aniso}} > 1$, meaning that the signal due to anisotropy is generally larger than the data uncertainties. In contrast, the percentage of modes with degree-2 observability larger than 1 is less than 40% for models SGLOBE-rani and SAW642ANb. From both Figs 3 and 4(a), we note that S362WMANI+M, savani and SPani are the models with the largest amplitudes of v_s anisotropy throughout the mantle, while SGLOBE-rani and SAW642ANb only contain large amplitudes in anisotropy at shallow depth or in the D″ region. As splitting function coefficients are calculated as a depth integral of the sensitivity kernel multiplied with the model values (see eq. 1), the larger model amplitudes of S362WMANI+M, savani and SPani are likely the reason why we find the highest number of modes with $O_2^{\text{aniso}} > 1$, as well as the highest values of observability for these models.

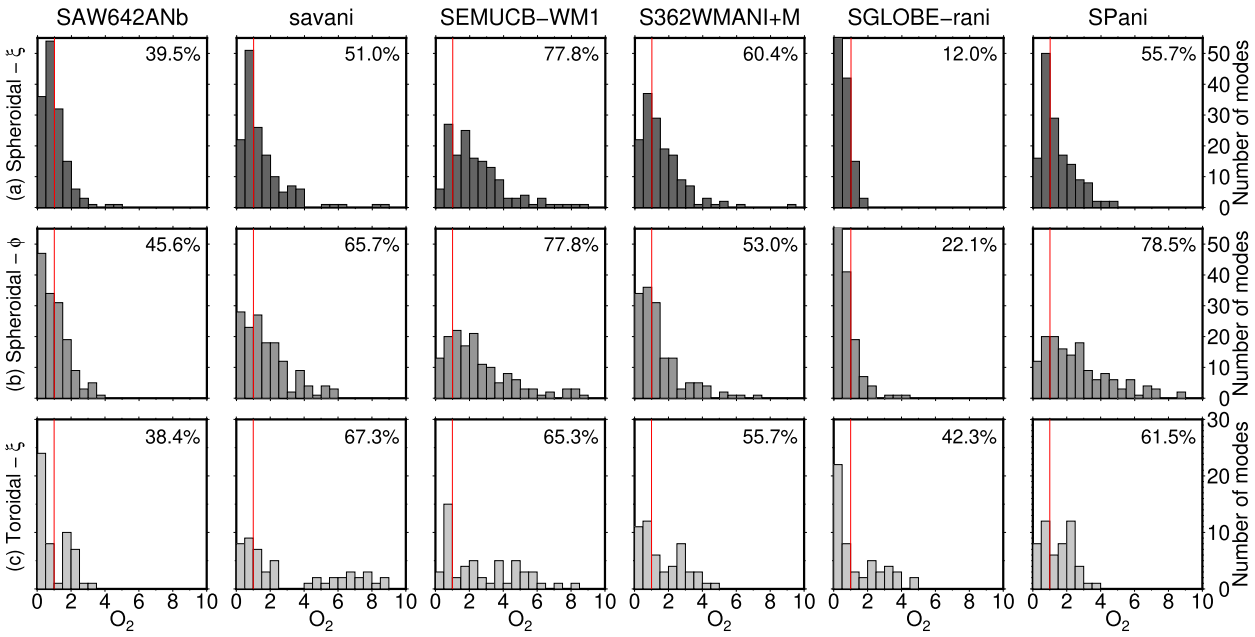

Figure 5. Histograms of v_s and v_p anisotropy observability (O_2^{aniso}) for spheroidal modes (top and middle rows, respectively) as well as v_s anisotropy observability for toroidal modes (bottom row), calculated for degree 2 structure using models SAW642ANb, savani, SEMUCB-WM1, S362WMANI+M, SGLOBE-rani and SPani (from left to right). The vertical red line indicates an observability value of 1. The number in the top-right corner of each panel indicates the percentage of modes with $O_2^{\text{aniso}} > 1$.

Generally, results for v_p anisotropy are similar to results for v_s anisotropy: high observability values and large numbers of modes with $O_2^{\text{aniso}} > 1$ are found for the same tomographic input models, but the percentage of modes able to see anisotropy is generally higher. This is likely due to the theoretical sensitivity of the data, as discussed further in Section 7. The percentage of toroidal modes with $O_2^{\text{aniso}} > 1$ across the different models is more consistent than when using spheroidal modes. This probably reflects the fact that toroidal modes are mainly sensitive to anomalies in the upper mantle (see examples of their sensitivity kernels in Fig. 2), where anisotropic tomography models show better agreement with each other.

Observability results for different spherical harmonic degrees (up to $s = 6$) are summarized in Fig. 6. 42–56% of the modes have $O_2^{\text{aniso}} > 1$ for at least 4 out of 6 models. However, these percentages decrease for higher degrees, especially for spheroidal modes, with only 10–20% of the modes able to see anisotropy at degree 4 or degree 6, respectively. Despite this decrease in sensitivity with increasing spherical harmonic degree s, there remain modes that are likely to observe both v_s and v_p anisotropy at least until degree 6. The fact that spheroidal modes show as high (or even larger) observability values for v_p anisotropy as for v_s anisotropy is promising for future work on v_p anisotropy. These analyses furthermore aid in identifying which normal modes to focus on in studies of mantle anisotropy, particularly when individual modes are studied in detail.

4.2 Anisotropy in different depth layers

To identify which normal modes are particularly useful for constraining radial anisotropy at specific depths, we confine anisotropy to certain depth ranges, leaving the rest of the mantle isotropic. Tables 1 and 2 summarize the results obtained for spheroidal and toroidal modes, respectively, listing the percentages of modes with $O_s^{\text{aniso}} > 1$ in each case (similar to the percentages indicated in Fig. 5).

For spheroidal modes (Table 1), the observability of v_s anisotropy decreases substantially below 670 km depth, actually vanishing in the lower mantle for models SAW642ANb and SGLOBE-rani. This is readily explained by Fig. 4(a), which shows that overall the anisotropy is maximum in the upper mantle and decreases in the lower mantle. For models SAW642ANb and SGLOBE-rani, there is negligible anisotropy in the lower mantle and thus we find v_s anisotropy observability values below the threshold of 1 from 670 km depth downwards. Although the observability also considers the data uncertainties, we thus find that the percentages in Table 1 mostly reflect the strength of the anisotropy in the input models.

Toroidal modes have the largest O_s^{aniso} values when anisotropy is present in the depth range 25–220 km, with about 40% of modes having observability values larger than 1. Again, the percentage of toroidal modes able to observe v_s anisotropy decreases with depth (Table 2). Only models S362WMANI+M and SEMUCB-WM1 have a number of modes with $O_s^{\text{aniso}} > 1$ for anisotropy below 670 km. When v_s anisotropy is restricted to a depth range in the mid or lower mantle, current toroidal mode data are not able to observe it. This is expected based on the toroidal modes considered here and their sensitivity kernels, which are mainly sensitive to v_{sh} in the upper mantle. Specific toroidal modes that are able to see anisotropy in the depth range 2500–2891 km are ${}_0T_8$ and ${}_3T_{16}$, both from the new toroidal mode data set of Schneider & Deuss (2021). In fact, about half of the new modes measured by (Schneider & Deuss 2021) show high observability values (specifically ${}_1T_{13}{-}{}_1T_{14}$, ${}_2T_{13}{-}{}_2T_{16}$, ${}_3T_{16}$) and are thus crucial to include in future studies of deep mantle anisotropy.

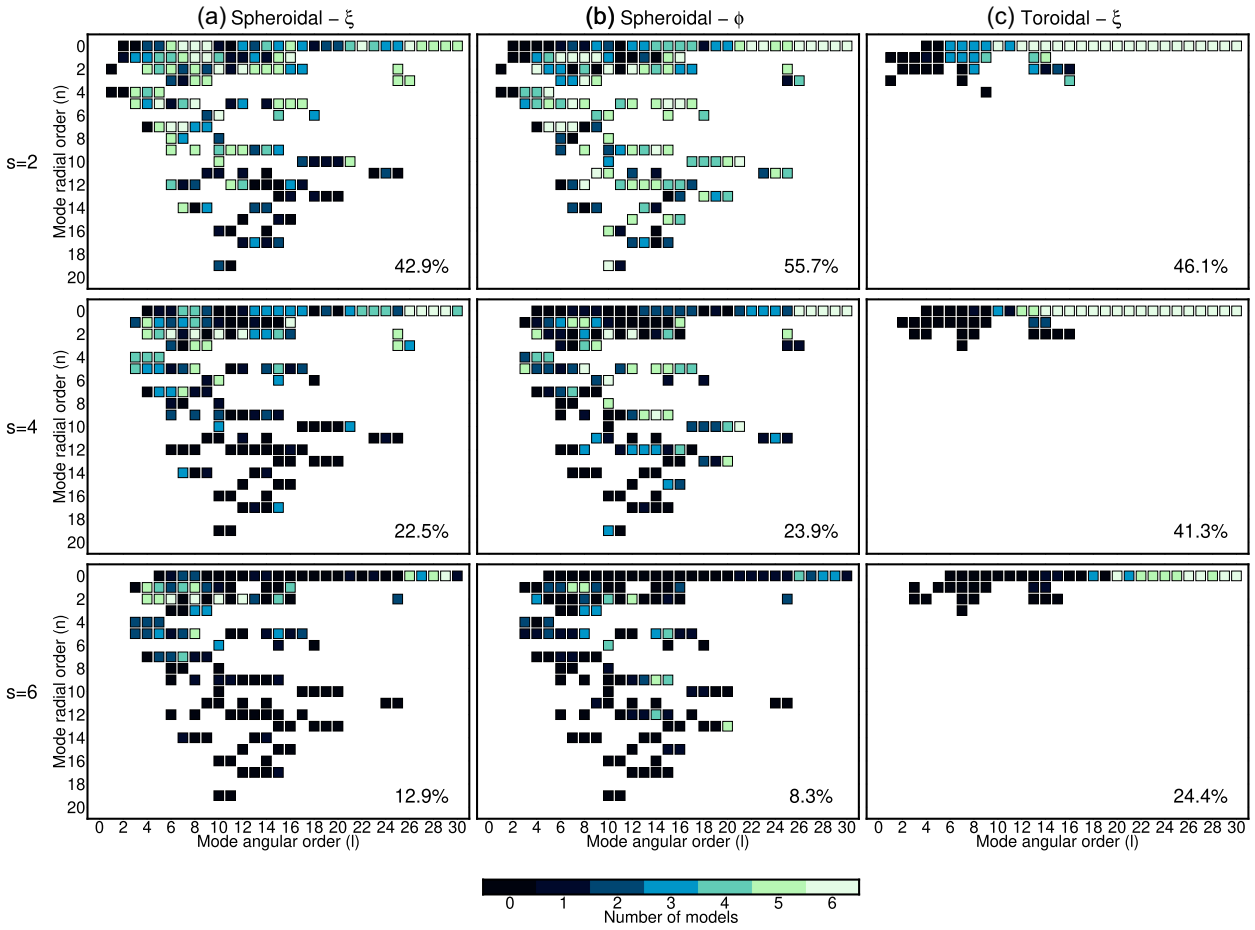

Figure 6. Plots summarizing O_s^{aniso} observability of (a,b) spheroidal modes and (c) toroidal modes to ξ and ϕ, respectively, for structure of degree 2 (top row), 4 (middle row) and 6 (bottom row). Each square represents a normal mode of radial and angular order n and l. The colour of each square indicates the number of models for which anisotropy observability is larger than 1. Thus, light colours indicate agreement between models on high anisotropy observability for each normal mode, dark colours indicate agreement on low observability for different normal modes. The number in the bottom-right corner of each panel indicates the percentage of modes with $O_s^{\text{aniso}} > 1$ for at least 4 out of 6 models.

Table 1. Percentage of spheroidal modes (out of a total of 149 modes) with O_2^{aniso} observability values for v_s anisotropy larger than 1. For each tomographic input model, we report the percentage of normal modes with $O_2^{\text{aniso}} > 1$ in case anisotropy is present in the whole mantle (all) or restricted to different depth ranges as indicated in the top row.

Model	All	25–220	220–400	400–670	670–1000	1000–1700	1700–2200	2200–2500	2500–2891	2741–2891
SAW642ANb	39.5	1.3	4.7	2.0	0	0	0	0	0	0
savani	51.0	18.7	4.0	9.4	2.7	0.7	7.4	8.7	21.4	0.7
SEMUCB-WM1	77.8	10.7	20.8	9.4	15.4	17.4	2.0	0	22.1	3.4
S362WMANI+M	60.4	5.4	6.0	12.7	19.4	1.3	14.0	0	4.0	0
SGLOBE-rani	12.0	16.1	1.3	6.0	0	0	0	0	0	0
SPani	55.7	2.0	8.7	6.7	0	1.3	12.7	14.0	14.0	0

Table 2. Percentage of toroidal modes (out of a total of 52 modes) with O_2^{aniso} observability values for v_s anisotropy larger than 1, for different depths in the mantle. Similar to Table 1.

Model	All	25–220	220–400	400–670	670–1000	1000–1700	1700–2200	2200–2500	2500–2891	2741–2891
SAW642ANb	38.4	32.6	25.0	0	0	0	0	0	0	0
savani	67.3	44.2	1.9	1.9	0	0	0	0	3.8	0
SEMUCB-WM1	65.3	38.4	40.3	5.8	3.8	3.8	0	0	3.8	0
S362WMANI+M	55.7	38.4	34.6	7.7	7.7	0	0	0	0	0
SGLOBE-rani	42.3	40.3	0	0	0	0	0	0	0	0
SPani	61.5	38.4	38.4	5.8	0	1.9	0	0	1.9	0

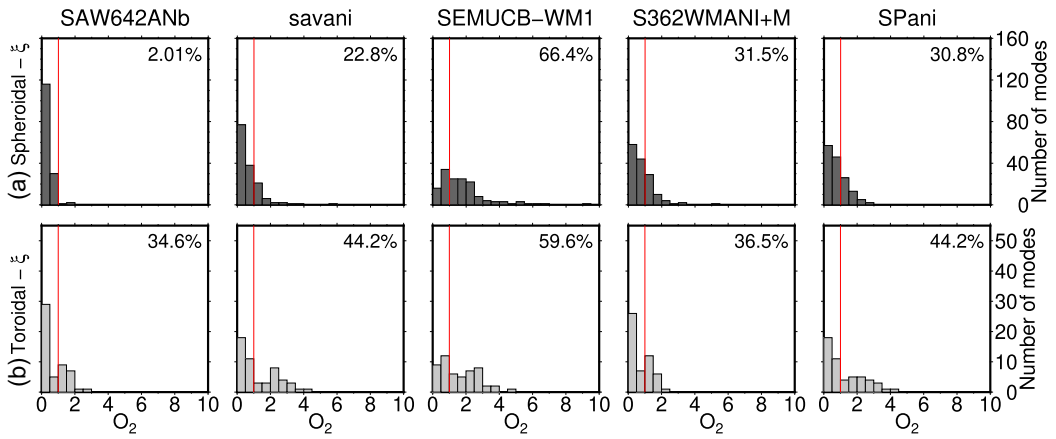

Figure 7. Histograms showing degree 2 observability values for different v_s anisotropy patterns (O_2^{pattern}), computed using the normalized anisotropic models indicated at the top with SGLOBE-rani as reference model. Similar to Fig. 5. Results for when anisotropy is only included in the top 220 km are given in Fig. S2.

4.3 Effect of lateral variations in anisotropy

In the previous section, we found that the observability results reflect to a large extent the strength of anisotropy in the input models. To investigate whether normal modes can distinguish between different patterns of anisotropy (lateral variations in anisotropy), we use the normalized input models (see Section 3.4) with results shown in Fig. 7. The percentage of spheroidal modes able to see lateral variations in v_s anisotropy varies substantially, from barely anything (2%) for model SAW642ANb to more than 65% for model SEMUCB-WM1. The latter is the model with the highest anisotropy amplitudes below 2000 km depth (Fig. 4), while reference model SGLOBE-rani has low anisotropy amplitudes. The low percentage for model SAW642ANb is likely due to the fact that, even after normalization, this model and SGLOBE-rani both effectively have no anisotropy below 670 km, making them very similar to each other (Fig. 4b). In Fig. S2 we also show results for normalized models with anisotropy only present between 25 and 220 km depth, where the radial average of ξ is similar across all the models. In this case, we observe similar observability values, with only 2–7% of spheroidal modes having O_s^{pattern} values larger than 1 (mostly the fundamental modes, as expected).

Percentages are visibly more consistent for toroidal modes, with on average 44% of normal modes able to distinguish between different anisotropy models. This is likely because most of the toroidal modes considered in this study are sensitive to shallow portions of the mantle, where all normalized models contain significant anisotropy. Nevertheless, the fact that different anisotropy models give rise to significant changes in the splitting functions for >40 % of currently observed normal modes stems us hopeful for future inversions of these normal mode data for mantle anisotropy.

4.4 Effect of crustal thickness

Observability results for crustal thickness are presented as histograms in Fig. 8, where we compare reference model CRUST2.0 to models CRUST1.0, CRUST5.1, CRUST-SG or CRUST-SEM (as described in Section 4). We find that normal modes are not able to distinguish model CRUST2.0 from either CRUST1.0 or CRUST5.1. This is due to the strong similarity of these models on the long wavelengths for which we have normal mode data (typically $s < 12$).

A higher percentage is obtained when comparing model CRUST2.0 with CRUST-SG with now 22.1% of spheroidal modes and 21.1% of toroidal modes having observability values above 1 for $s = 2$. As expected, most of these modes are fundamental modes that are most similar to surface waves. Although we obtain an even higher percentage of modes with O_2^{crust} values above 1 for CRUST-SEM, this is slightly misleading, as this model is built as an 'equivalent model' and not necessarily realistic. We note that the observability for CRUST-SEM is never greater than one for the CMB Stoneley modes, which therefore are not substantially affected by the use of very different crustal models.

5 TRADE-OFFS BETWEEN RADIAL ANISOTROPY AND OTHER STRUCTURES

So far we have considered how strong anisotropy in the mantle has to be to be observable in current normal mode data. However, the seismic detection of anisotropy in the mantle is also complicated by possible trade-offs with other structures, which may mask the presence of anisotropy or give rise to larger amplitudes in models. Therefore, we investigate here whether significant trade-offs exist between radial anisotropy and other structures, particularly crustal thickness variations and the compressional wave velocity structure of the mantle.

To investigate possible trade-offs, we compare synthetic splitting functions to a set of reference predictions using the isotropic part of model SEMUCB-WM1 combined with crustal model CRUST-SEM and a constant v_p scaling factor ($\delta \ln v_p = 0.5 \times \delta \ln v_s$). We choose this model as it is the model with the largest overall observability to v_s anisotropy, making it easier to identify possible trade-offs between anisotropy and other features. We test the effect of anisotropy, crustal thickness and v_p scaling by calculating synthetic splitting function coefficients for this reference case (i) with the addition of the anisotropic part of SEMUCB-WM1, (ii) using CRUST2.0 instead of CRUST-SEM to describe crustal thickness variations and (iii) using a depth-dependent v_p scaling instead of a constant scaling, which decreases linearly from 0.5 at the surface to 0.33 at the core-mantle boundary (as used in Ritsema *et al.* 2011).

Fig. 9 shows examples of splitting function predictions for two coefficients (c_{20} and $\Re(c_{22})$, focusing on core–mantle boundary Stoneley modes, where $\Re$ denotes the real part of the coefficient.

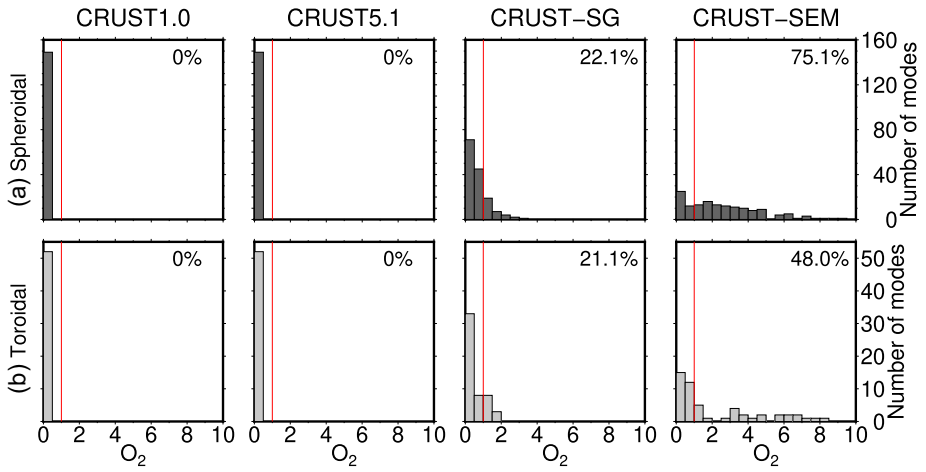

Figure 8. Histograms of degree 2 observability values for different crustal thickness models (O_2^{crust}), comparing predictions for reference model SGLOBE-rani combined with CRUST2.0 to predictions for SGLOBE-rani with the crustal thickness model indicated at the top for (a) spheroidal and (b) toroidal modes. Similar to Fig. 5.

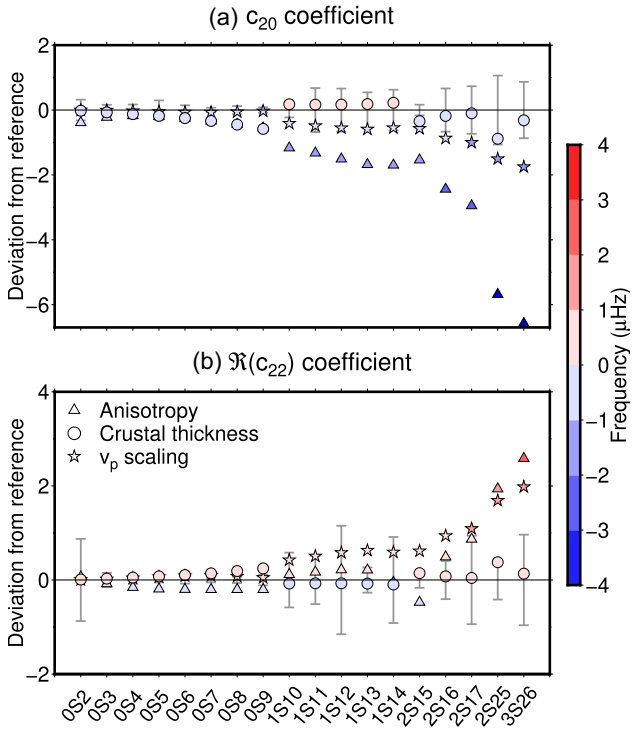

Figure 9. Predictions for Stoneley mode splitting functions for the c_{20} and real c_{22} coefficient [denoted $\Re(c_{22})$] relative to predictions for isotropic SEMUCB-WM1 with CRUST-SEM on top. We compare predictions for anisotropic SEMUCB-WM1 with CRUST-SEM (triangles), isotropic SEMUCB-WM1 with CRUST2.0 (circles) and isotropic SEMUCB-WM1 with CRUST-SEM and a depth-dependent v_p scaling (stars), which are all coloured by the deviation from the reference case predictions (in μHz). When predictions fall on the same side of zero, there is no trade-off between the respective structures, while there may be a trade-off if they fall on opposite sides of zero. Grey bars indicate the amplitude of the data uncertainties (centred around zero), to visualize how significant the effect of different structures are compared to these. The degenerate frequency of the modes increases along the x-axis and their sensitivity becomes progressively more focused to the CMB.

Changing the crustal thickness model has little effect on these lower mantle sensitive normal modes, with the change from the reference predictions being smaller than the data uncertainties in most of the cases. In contrast, the presence of anisotropy and the use of a different v_p scaling both introduce frequency variations significantly larger than the data uncertainties, with the effect being stronger for modes with increasing frequency and thus increasing sensitivity to the CMB. Importantly, for these coefficients (which together strongly contribute to the characteristic 'Ring around the Pacific' pattern observed in lower mantle tomography models), we do not identify a large trade-off between anisotropy and crustal thickness or compressional wave velocity structure (i.e. the deviations in mode frequencies are either both negative or both positive).

Figs 10 and 11 generalize our results from Fig. 9 to all spheroidal and toroidal modes, respectively, plotting the deviation in frequency due to the effect of anisotropy, changing the crustal thickness model or v_p scaling for all degree 2 coefficients. Equivalent results for degree 4 coefficients are shown in Fig. S3. For fundamental modes that resemble surface waves ($n = 0$, high l), we identify a trade-off between anisotropy and crustal thickness for most degree 2 coefficients, as expected. Other modes show mostly a trade-off between anisotropy and crustal thickness for coefficient c_{20} (though not between anisotropy and v_p scaling), but importantly not for any of the Stoneley modes as discussed before. If, instead of these two quite different crustal thickness models, we compare CRUST-SG and CRUST2.0 (see Fig. S4), the effect of crustal thickness is significantly smaller and does not lead to trade-offs with anisotropy for lower mantle sensitive modes.

For modes with $n > 0$, the trade-offs between anisotropy and v_p structure are more significant, particularly for coefficients $\Re(c_{22})$ and $\Im(c_{22})$, e.g. see modes ${}_8S_6$, ${}_{10}S_{21}$ and ${}_{12}S_{16}$. This implies that during inversions for mantle anisotropy it will be important to consider the influence of the v_p structure and carefully consider what scaling to use between v_s and v_p. For toroidal modes (Fig. 11), we do not observe any trade-offs between anisotropy and crustal thickness or v_p scaling.

The results shown so far are computed using model SEMUCB-WM1. As different models have different amplitudes and patterns of anisotropy, the use of a different model may give rise to a stronger or weaker effect of anisotropy on normal modes, thus leading to

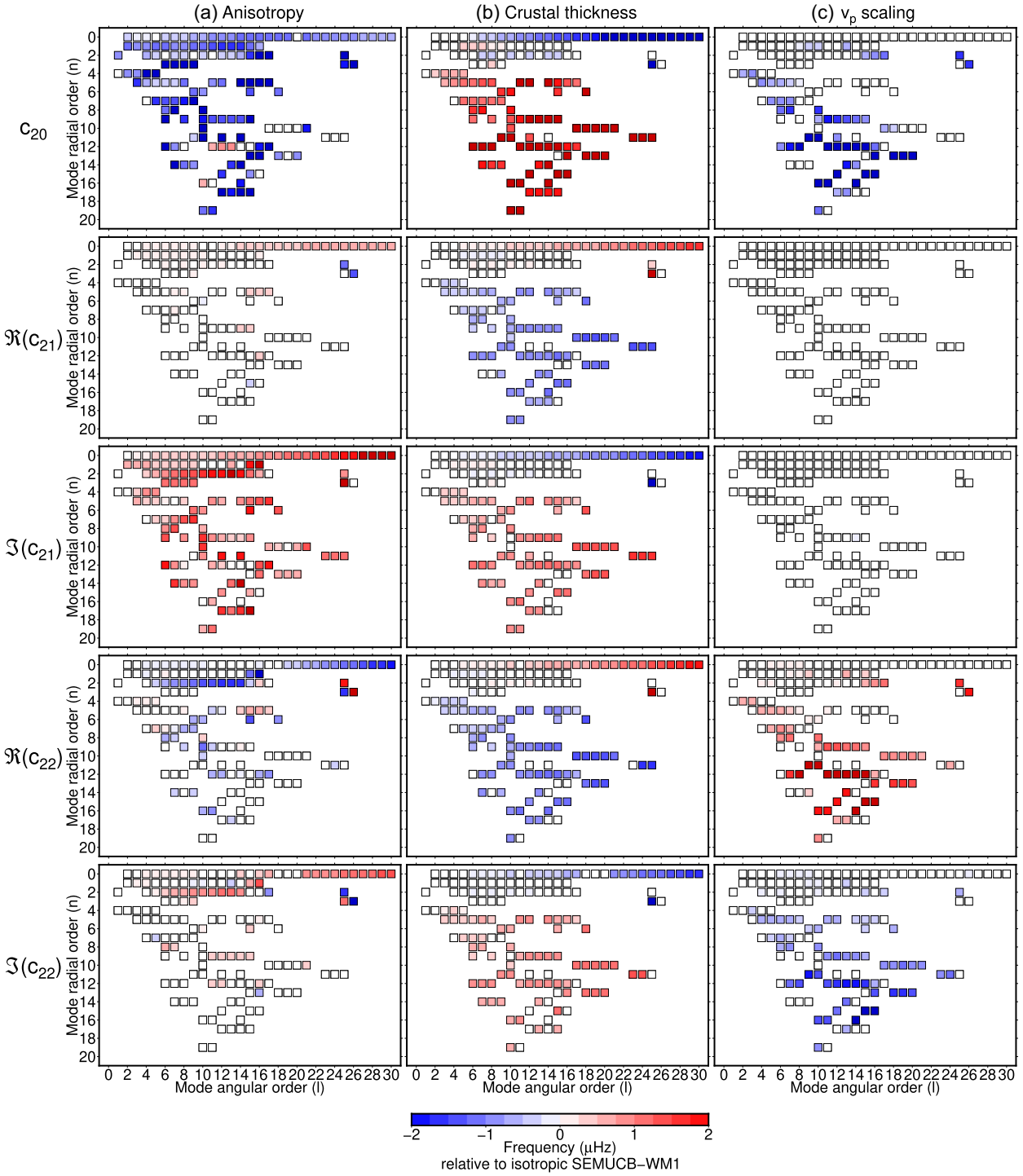

Figure 10. Effect of different structures in the mantle on the frequencies of spheroidal modes for degree 2 including results for real ($\Re$) and imaginary ($\Im$) coefficients. Results for degree 4 are shown in Fig. S3. We plot splitting function coefficients relative to predictions for isotropic SEMUCB-WM1 with crustal thickness variations according to CRUST-SEM and a constant v_p scaling factor ($\delta \ln v_p = 0.5 \times \delta \ln v_s$). In the different columns, we show the effect of (a) including v_s anisotropy, (b) changing the crustal thickness model to CRUST2.0 and (c) changing the v_p scaling to be depth-dependent (as described in the text). Each square represents a particular normal mode, with the colour indicating the deviation in frequency (as in Fig. 9). Trade-offs exist when opposite colours (red or blue) are observed between columns as these frequency shifts may cancel each other out. Squares are coloured white when the frequency shift from the reference case is smaller than the data uncertainty and thus not significant for that particular normal mode.

different results. Fig. S4 shows equivalent results to Fig. 10, now using model SGLOBE-rani with CRUST-SG as reference case. In this case, it is noticeable that anisotropy has a smaller effect on normal modes due to the smaller model amplitudes, with the effect of crustal thickness also smaller, as explained above. We observe roughly the same effect due to a different v_p scaling when using models SEMUCB-WM1 and SGLOBE-rani. Despite these slight differences between Fig. 10 and Fig. S4, it is important to note

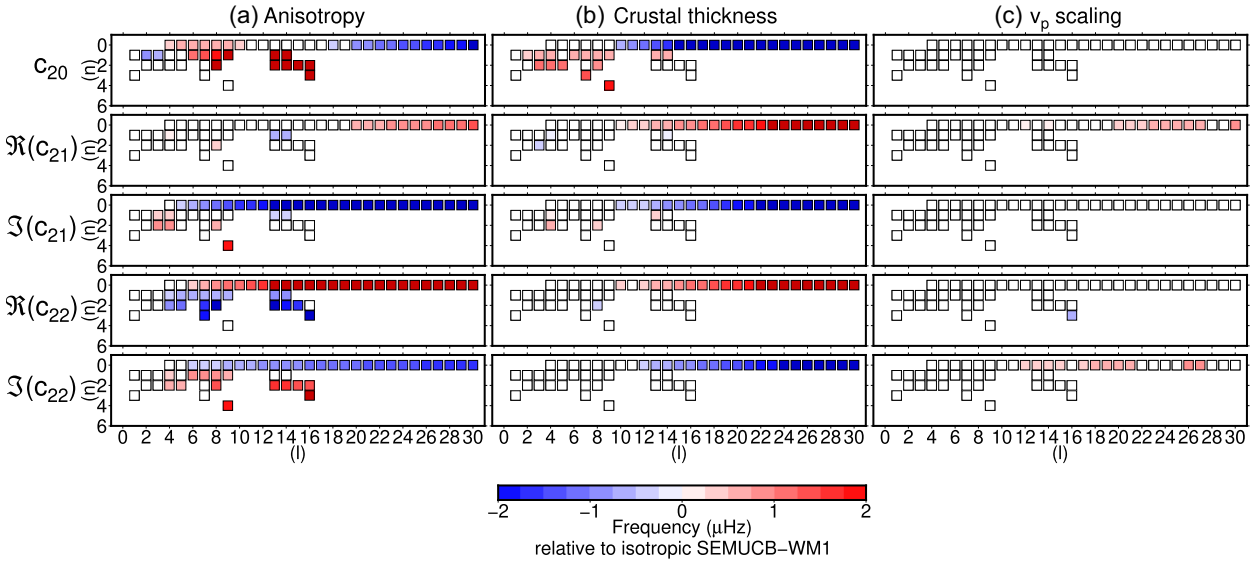

Figure 11. Effect of different structures in the mantle on the frequencies of toroidal modes, showing all coefficients for degree 2, including results for real ($\Re$) and imaginary ($\Im$) coefficients. We compare the effect of (a) anisotropy, (b) crustal thickness and (c) v_p scaling on individual normal modes. Trade-offs may exist when colours are opposite between different columns. See the caption of Fig. 10 for more details.

that we never identify a trade-off between anisotropy and crustal thickness for the Stoneley modes.

6 MISFIT RESULTS

Although it is not the intention of this work to inform about the present-day radial anisotropy structure of the mantle, it is interesting to look at the fit of existing tomographic models to current normal-mode data. We discuss these misfit results in Tables 3 and 4 for spheroidal modes and in Table S2 for toroidal modes. Although there are exceptions, we can identify some trends in the results as detailed below.

When the mantle is considered to be isotropic, SGLOBE-rani is the model with the lowest overall misfit for spheroidal modes, irrespective of whether we consider structure at $s = 2$ or all degrees (Table 3). With the addition of anisotropy, the predictions obtained using SGLOBE-rani still fit the observations better than those of any other model, when all spheroidal modes are considered. If we consider only fundamental or Stoneley modes separately, model S362WMANI+M, which was developed using normal mode data, performs best. SGLOBE-rani still shows low misfit values for fundamental modes (which are similar in sensitivity to the surface waves used to construct the model), but the fit gets significantly worse when we consider Stoneley modes. Overall, we note that for anisotropic models, the misfit of fundamental mode observations is lower than that to Stoneley mode observations, fitting with our expectation that anisotropic structure in the lowermost mantle is not well constrained. The addition of anisotropy does not always improve the overall data fit though, in particular for models SAW642ANb, S362WMANI+M and SGLOBE-rani. This does not necessarily mean that mode data prefer the isotropic model, but more likely indicates that the patterns and amplitude of anisotropy in these tomography models still have to be improved in order to fit normal mode data, particularly in the lower mantle. Misfit results for toroidal modes (Table S2) are consistent with these findings, showing that predictions for SGLOBE-rani fit the observations best, both with and without anisotropy.

As discussed in Sections 3.3 and 4.4, the Moho depths of CRUST-SEM are not realistic in the oceans, where they are set to 30 km. This could have an effect on the misfit for SEMUCB-WM1 predictions reported above. We test this by calculating the data misfit using predictions for SEMUCB-WM1 combined with CRUST2.0. As comparison we also show results for when we change the crustal model for the two best performing models S362WMANI+M and SGLOBE-rani, by using CRUST5.1 and CRUST2.0, respectively. Given the strong effect of the v_p scaling on normal mode frequencies (see Section 5), we also compare the effect of changing the v_p scaling on these misfit results (using a depth-dependent scaling factor again). Table 4 shows that the misfit for SEMUCB-WM1 indeed improves when we use CRUST2.0, though not by very much. Changing the crustal thickness model for S362WMANI+M does not change the misfit, while it has a small effect on the misfit for SGLOBE-rani. The use of a depth-dependent v_p scaling further improves the fit for SEMUCB-WM1 and S362WMANI+M, but not for SGLOBE-rani.

7 DISCUSSION

We have used the concept of observability and misfit calculations to investigate the sensitivity of normal modes to global anisotropic mantle structure. By using a number of global tomography models, by considering several scenarios of anisotropy and by analysing all lower mantle normal modes for which measurements are available since 1995, this study goes beyond the work of Koelemeijer *et al.* (2012) who introduced the concept of normal mode observability. Using predictions for existing anisotropic tomography models, we have shown that normal modes are able to provide valuable constraints on both v_s and v_p anisotropy in the mantle and can distinguish between existing anisotropic tomography models based on our misfit results. Here, we will discuss some of our key findings as well as some limitations of our approach, before we finish by discussing implications for future inversions of mantle structure.

Table 3. Misfit to spheroidal mode observations for splitting function predictions calculated using models SAW642ANb, savani, SEMUCB-WM1, S362WMANI+M, SGLOBE-rani and SPani. In the different columns we compare the misfit for isotropic predictions for all modes (Iso - All), anisotropic predictions for all modes (Aniso - All), as well as anisotropic predictions for fundamental modes only (Aniso - Fundamental) or Stoneley modes only (Aniso - Stoneley). In each case, we show the misfit for degree 2 only ($s = 2$) or all degrees together (s =all, up to $s = 12$). Values in bold indicate the lowest misfit in each column.

Model	Iso - All		Aniso - All		Aniso - Fundamental		Aniso - Stoneley	
	$s = 2$	s =all	$s = 2$	s =all	$s = 2$	s =all	$s = 2$	s =all
SAW642ANb	7.72	2.55	6.91	2.42	8.86	4.13	11.98	2.97
savani	17.21	4.45	14.60	3.88	24.00	5.77	46.68	11.52
SEMUCB-WM1	6.96	2.36	6.08	2.25	7.91	2.45	7.56	2.85
S362WMANI+M	5.00	1.87	5.77	2.01	**4.77**	**1.79**	**7.32**	**1.96**
SGLOBE-rani	**4.06**	**1.75**	**4.23**	**1.79**	4.79	2.40	12.45	3.19
SPani	6.67	2.27	6.49	2.12	12.96	3.41	28.45	6.39

Table 4. Misfit to spheroidal mode observations for splitting function predictions calculated using models SEMUCB-WM1, S362WMANI+M and SGLOBE-rani. In the different columns we compare misfit values for predictions using the original models, that is SEMUCB-WM1, S362WMANI+M and SGLOBE-rani with, respectively, CRUST-SEM, CRUST2.0 and CRUST-SG on top and a constant v_p scaling factor (Case = 'Original'), the original models with a different crustal thickness model, that is CRUST2.0 for SEMUCB-WM1 and SGLOBE-rani and CRUST5.1 for S36WMANI+M (Case = 'Crustal thickness'), and the original models with a depth dependent v_p scaling factor (Case = 'v_p scaling'). In each case, we show the misfit for degree 2 ($s = 2$) and all degrees together (s =all, up to $s = 12$), and for the isotropic parts of the models as well as the full anisotropic model using all modes. Values in bold indicate the lowest misfit for each model and column.

Model	Case	Iso - All		Aniso - All	
		$s = 2$	s =all	$s = 2$	s =all
SEMUCB-WM1	Original model	6.96	2.36	6.08	2.25
	Crustal thickness	6.75	2.36	**5.51**	2.19
	v_p scaling	**6.46**	**2.23**	5.86	**2.17**
S362WMANI+M	Original model	5.00	1.87	5.77	2.01
	Crustal thickness	5.00	1.87	5.77	2.02
	v_p scaling	**4.18**	**1.67**	**4.76**	**1.77**
SGLOBE-rani	Original model	4.06	1.75	**4.23**	1.79
	Crustal thickness	**4.04**	**1.67**	4.35	**1.77**
	v_p scaling	4.35	1.72	4.59	1.81

7.1 Limitations

Rather than considering the theoretical sensitivity of normal modes, our approach utilizes the uncertainties of current normal mode data. We believe this provides more useful insights than a study of mode sensitivity kernels, which we have also included for completeness in the Supporting Information (Fig. S5).

A limitation of this approach is that results depend on currently available normal mode data and their associated uncertainties. Consequently, results may change when normal mode splitting coefficients and their uncertainties are re-evaluated (though generally only for the better). For example, the new measurements from Schneider & Deuss (2021) significantly improved the observability of toroidal mode data sets, not only by expanding the data sets with new overtone measurements, but also by improving older measurements based on new seismic spectra, most of which now have lower uncertainties.

Another limitation is given by the fact that we base our observability calculations on existing tomographic models. We prefer this approach nevertheless, as such tomographic models are at least constrained by observations. However, this does limit us, as the results depend on the characteristics of the models themselves, which for example never have large anisotropy variations in the mid or lower mantle. Since we do not know for certain whether any of these models inform us about the actual anisotropic structure of the Earth, we base our study on six tomography models that contain a different distribution and strength of anisotropy. An alternative would be to base our analysis on synthetic tomography models derived from geodynamic mantle circulation models that are constrained by physical processes. While these may be unaffected by regularization choices and thus have stronger amplitudes, they would still come with a range of issues, such as the choice of mineralogy and deformation mechanism and the need for plate reconstructions to obtain a realistic distribution of mantle heterogeneity.

Finally, we have used first-order perturbation theory throughout this work, including for our calculations of crustal thickness corrections. This seems justified given the wavelengths of normal modes relative to the thickness of the crust. However, we have not explicitly investigated this assumption. With the advance of spectral element methods that include self-gravitation (e.g. Kemper *et al.* 2022), it may be possible to test these assumptions in future studies.

7.2 Observability of radial anisotropy amplitudes and patterns

We have attempted to investigate the observability of both the strength of anisotropy as well as its pattern (or the lateral variations in anisotropy). Due to the presence of strong anisotropy at shallow depth in all the models (radial average always larger

than 1.06, Fig. 4a), normal modes are able to observe anisotropy when anisotropy is present in the entire mantle. When investigating anisotropy only in the lower mantle, it appears that the radial average of ξ needs to be larger than around 1.005 (radially averaged amplitude of anomalies is roughly 0.5%) to have a significant effect on normal modes. We base this on the fact that in SGLOBE-rani, one of the models with the weakest anisotropy, v_s anisotropy has a negligible effect on most of the modes (Fig. S4a), while anisotropy in SEMUCB-WM1 is strong enough to cause significant changes in the splitting function coefficients (Fig. 10a).

We have used input models with normalized amplitudes to investigate the impact of different patterns of anisotropy, finding that on average ∼31% of spheroidal modes and ∼44% of toroidal modes can distinguish between different global anisotropy models (Fig. 7). When restricting the anisotropy to specific depths only, specifically between 25 and 220 km depth, where $\xi > 1$ is similar across all normalized models (Fig. 4b), we find that only ∼5% of spheroidal modes have observability values larger than 1 (compared to 36% for toroidal modes, Fig. S2). As the percentage for spheroidal modes is consistently small, the large range of percentages found for anisotropy in the whole mantle (Fig. 7) is likely due to differences in anisotropy amplitude deeper in the mantle, which are still present after normalization. In contrast, for the toroidal modes we always observe observability values larger than 1 for more than 30% of modes, as these modes are mostly sensitive to the shallow mantle where anisotropy models are consistent. It is not possible to repeat this exercise for anisotropy just in the lowermost mantle, as the sign of the radially averaged anisotropy varies between models (see Fig. 4b). This prevents us from normalizing anisotropy model amplitudes just in the deep mantle and we are thus not able to assess whether the pattern of anisotropy in the lowermost mantle is observable based on these tomographic models.

An important finding of our study is that the observability to v_p anisotropy is generally higher than the v_s anisotropy observability. If the normal modes we considered had equal sensitivity to v_s and v_p anisotropy, the observability should only depend on the relative amplitudes of v_s and v_p. This should result in a higher observability for v_s anisotropy since $\delta \ln v_p \sim 0.5 \times \delta \ln v_s$, which is not what we observe. Given that the data uncertainties are the same, we can thus conclude that our normal mode data set has an overall larger sensitivity to v_p anisotropy than to v_s anisotropy. This can be verified by considering the theoretical sensitivity kernels of the modes we have analysed here. Fig. S5 summarizes the overall sensitivity of each mode to overall mantle anisotropy. We find that our data set of spheroidal modes is sensitive to v_{sv}, while it shows significant sensitivity to both v_{ph} and v_{pv}. This sensitivity mostly arises from measurements of *P*-wave sensitive modes by Deuss *et al.* (2013) and Koelemeijer *et al.* (2013), which have already enabled independent inversions for both shear wave and compressional wave structure (Koelemeijer *et al.* 2016) and now also pave the way for inversions for compressional wave anisotropy.

Throughout this study, we have separately considered results for different spherical harmonic degrees. To discuss the overall effect of anisotropy and crustal thickness on normal modes, it is useful to combine all degrees in splitting function maps, which ultimately serve as data for tomographic inversions. As example, Fig. 12 shows the observed and predicted splitting function maps for lower mantle mode ${}_1S_{14}$, for which sensitivity kernels are given in Fig. 2(c). We observe negligible differences between the splitting functions predictions of this lower mantle mode for different crustal thickness models, consistent with our conclusions in Section 5 based on Fig. 10. On the contrary, different anisotropic models lead to

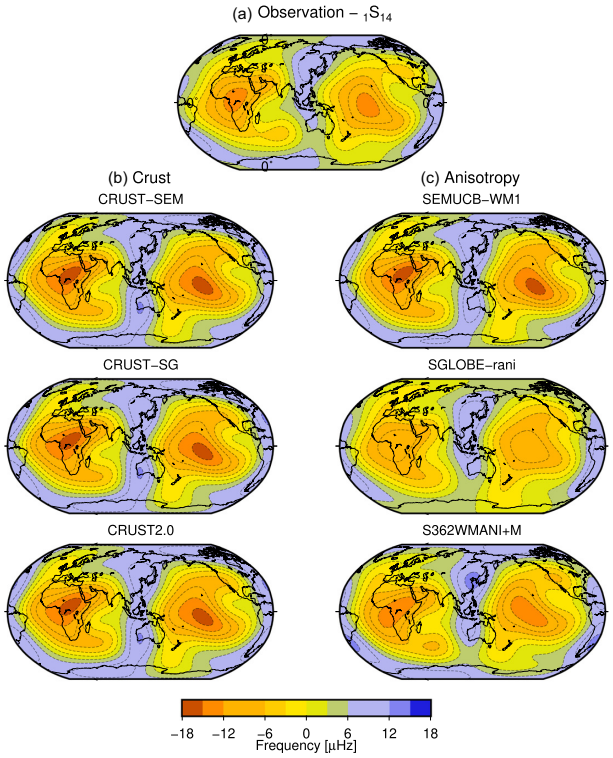

Figure 12. Observed and predicted splitting function maps for mode ${}_1S_{14}$ plotted up to spherical harmonic degree 6. (a) Observed splitting function from Koelemeijer *et al.* (2013). (b) Predicted splitting functions for isotropic SEMUCB-WM1 with different crustal thickness models, showing CRUST-SEM (top), CRUST-SG (middle) and CRUST2.0 (bottom). (c) Predicted splitting functions for anisotropic models SEMUCB-WM1 (top), SGLOBE-rani (middle) and S362WMANI+M (bottom), respectively, with CRUST-SEM, CRUST-SG and CRUST2.0 on top.

visually different predictions, particularly changing the amplitude of the predicted splitting function. Consistent with our misfit results (see Table 3), model S362WMANI+M visually resembles the observation best, while SEMUCB-WM1 and SGLOBE-rani over- and underestimate the amplitude, respectively. Equivalent examples are given in Figs S6 and S7 for modes ${}_0S_{26}$ and ${}_2T_7$. The predictions of fundamental mode ${}_0S_{26}$ are visually different when changing either the crustal thickness model or the anisotropy structure of the mantle. This is consistent with previous studies (e.g. Marone & Romanowicz 2007; Bozdağ & Trampert 2008; Ferreira *et al.* 2010) as these high frequency fundamental normal modes are equivalent to surface waves.

7.3 Data misfit

Although not the primary aim of this study, the misfit results provide some interesting insights. Tomography model S362WMANI+M is the only model considered here that included normal-mode data in its construction and it is thus not surprising it fits real data well. For the other five models considered, normal modes represent a way to independently assess the fit of the model to new data. From these five, SGLOBE-rani fits the normal mode data best (except when we consider Stoneley modes only). This is likely due to two reasons: (1) SGLOBE-rani has been built using ∼43 million surface wave measurements, which are similar to normal modes at higher frequencies and (2) SGLOBE-rani is also parametrized in spherical harmonics, which are natural basis functions for the normal modes.

Model SEMUCB-WM1 also performs relatively well, particularly when we consider Stoneley modes, while models savani and SPani typically have a poor data fit, likely due to the fact that these were constructed using higher-frequency body waves only. The fact that we consistently find lower misfit values for fundamental modes than Stoneley modes indicates that anisotropic models in the lowermost mantle still need to be improved, while anisotropy in the upper mantle is better constrained in current tomographic models.

7.4 Implications for tomographic inversions

Normal mode data are not as routinely included in tomographic inversions as body waves and surface waves. Up to date, only the studies by Moulik & Ekström (2014) and Moulik & Ekström (2016) have included normal mode splitting functions in inversions for 3-D radial anisotropy in the mantle. These studies found that the inclusion of splitting function data in their data set helped to reduce (but not remove) the trade-off between isotopic and anisotropic structures in the lower mantle (Moulik & Ekström 2014). It will be interesting to see whether these trade-offs can be entirely removed when only normal mode data are used in inversions.

There appears to be a link between between our observability results and the normal mode data fit of Moulik & Ekström (2014, 2016). Typically, for modes for which we find a high observability, such as ${}_0S_8$, ${}_1S_9$, ${}_2S_{10}$ and ${}_{10}S_{21}$ (Fig. 6), they also found a good model fit, while modes with low observability values (e.g. ${}_0S_2$, ${}_1S_2$, ${}_{12}S_7$ and ${}_2T_2$) showed poor data fits. Naturally, not all modes follow this first order trend (e.g. ${}_4S_3$, ${}_0T_{10}$), likely due to the fact that Moulik & Ekström (2014) also included other types of data.

Our splitting function predictions for different mantle structures indicate a trade-off between anisotropy and compressional wave velocity structure (Fig. 10). As both affect the splitting functions to a similar extent, and will change the fit to the data (Table 4) we cannot neglect the compressional wave velocity structure of the mantle in inversions for anisotropy. Future studies should thus carefully consider the choice of scaling between shear and compressional wave structure. Ideally, such studies should use inverse methods that are able to incorporate uncertainties from unmodelled structures in the mantle, such as the SOLA method (Subtractive Optimally Localized Averages, Zaroli 2016), which is based on Backus–Gilbert theory (e.g. Backus & Gilbert 1967, 1968). In this type of inverse method, the sensitivity of normal modes to v_p could be treated as additional '3-D' noise, when inverting for v_s anisotropy.

Our forward modelling results also provide insights into the depth resolution we may expect to obtain in global inversions. Normal modes are generally not able to observe anisotropy if it is present only in the bottom 150 km of the mantle (last columns of Tables 1 and 2). A larger number of modes have observability values larger than 1 when we increase the thickness of this anisotropic layer to roughly 400 km (second last columns in the same tables). It is thus unlikely that normal mode data are able to constrain anisotropy variations in just the bottom 150 km of the mantle.

The fact that existing tomographic models lead to substantially different predictions (Section 4) and misfit values (Section 6) suggests that there is sufficient sensitivity in existing normal mode data to mantle anisotropy on long wavelengths, where models continue to disagree. Although the resolving power of normal modes may be lower than that of other data types, this indicates they are important complementary data to include in studies of mantle anisotropy. We particularly encourage the community to utilize the recent measurements of toroidal mode overtones by Schneider & Deuss (2021) in tomography inversions, as these show significant sensitivity to v_s anisotropy in the deep mantle (Fig. 5) and are fit reasonably well by existing tomographic models (Fig. S7).

8 CONCLUSIONS

Anisotropy is an important seismic quantity that, if constrained accurately, provides important information on mantle flow. In this study, we have investigated the sensitivity of current normal mode data to radial anisotropy in the mantle using existing global tomographic models. On the one hand, we have used the concept of observability to determine to which extent normal modes are able to resolve the Earth's anisotropic structure at different depths and with different patterns. On the other hand, we have investigated how well existing tomographic models fit current normal mode data. We believe these forward modelling results provide useful insights for future inversions of normal mode data for mantle anisotropy.

Specifically, we find that on average about 50% of spheroidal modes and 55% of toroidal modes investigated here show significant sensitivity to v_s anisotropy in the mantle. Importantly, roughly 57% of spheroidal modes are also sufficiently sensitive to v_p anisotropy, which remains completely unconstrained in the mantle. While results depend on the characteristics of the tomographic input models, different anisotropy models lead to visually different splitting functions and misfit values. While all models considered here produce a reasonable fit to fundamental normal mode measurements, the fit to Stoneley modes varies significantly, indicating that there is scope to improve anisotropic tomographic models in the lower mantle using normal mode data.

We find that, in contrast to findings for body waves and surface waves, crustal thickness corrections have no strong impact on lowermost mantle sensitive normal modes, except when we use a crustal thickness model with unrealistic crustal thicknesses in the oceans. However, splitting function predictions are changed to a similar extent by v_s anisotropy and isotropic v_p structure, affecting the fit to the data. Given these trade-offs, inversions for v_s anisotropy should not neglect the compressional wave velocity structure of the mantle, and the choice of scaling value between shear- and compressional wave velocity structure would require careful consideration. Nevertheless, our finding that current normal mode data sets provide significant sensitivity to both v_s and v_p anisotropy makes future studies of v_p anisotropy of the mantle feasible.

ACKNOWLEDGMENTS

The authors are grateful to the editor Gabi Laske, and reviewers Barbara Romanowicz and Rudolf Widmer-Schnidrig for their constructive comments that improved the quality of the paper. We are also grateful to all members of the community who have enabled this work by making their tomographic and crustal models available, as well as those who have shared their normal mode splitting functions measurements publicly. FR received funding from Royal Society grants RGF\EA\181029 and RF\ERE\210182 awarded to PK and gratefully acknowledges their support. PK acknowledges support from a Royal Society University Research Fellowship (URF\R1\180377). AF is supported by NERC grant NE\N011791\1. All figures were produced using the GMT software (Wessel *et al.* 2013).

DATA AVAILABILITY

The computed splitting function predictions as well as a plotting script to visualize these are made available online: https://doi.org/10.5281/zenodo.7101457 (Restelli *et al.* 2022).

REFERENCES

Anderson, D.L., 1961. Elastic wave propagation in layered anisotropic media, *J. geophys. Res.,* **66**(9), 2953–2963.

Auer, L., Boschi, L., Becker, T., Nissen-Meyer, T. & Giardini, D., 2014. Savani: a variable resolution whole-mantle model of anisotropic shear velocity variations based on multiple data sets, *J. geophys. Res.,* **119**(4), 3006–3034.

Babuska, V. & Cara, M., 1991. *Seismic Anisotropy in the Earth,* Vol. **10,** Springer Science & Business Media.

Backus, G. & Gilbert, F., 1968. The resolving power of gross earth data, *J. geophys. Int.,* **16**(2), 169–205.

Backus, G.E., 1962. Long-wave elastic anisotropy produced by horizontal layering, *J. geophys. Res.,* **67**(11), 4427–4440.

Backus, G.E. & Gilbert, J., 1967. Numerical applications of a formalism for geophysical inverse problems, *J. geophys. Int.,* **13**(1–3), 247–276.

Bassin, C., Laske, G. & Masters, G., 2000. The current limits of resolution for surface wave tomography in North America, *EOS, Trans. Am. geophys. Un.,* **81,** F897

Bozdağ, E. & Trampert, J., 2008. On crustal corrections in surface wave tomography, *J. geophys. Int.,* **172**(3), 1066–1082.

Chang, S.-J. & Ferreira, A.M., 2017. Improving global radial anisotropy tomography: the importance of simultaneously inverting for crustal and mantle structure, *Bull. seism. Soc. Am.,* **107**(2), 624–638.

Chang, S.-J., Ferreira, A.M., Ritsema, J., van Heijst, H.J. & Woodhouse, J.H., 2014. Global radially anisotropic mantle structure from multiple datasets: a review, current challenges, and outlook, *Tectonophysics,* **617,** 1–19.

Chang, S.-J., Ferreira, A.M., Ritsema, J., Heijst, H.J. & Woodhouse, J.H., 2015. Joint inversion for global isotropic and radially anisotropic mantle structure including crustal thickness perturbations, *J. geophys. Res.,* **120**(6), 4278–4300.

Chang, S.-J., Ferreira, A.M. & Faccenda, M., 2016. Upper-and mid-mantle interaction between the Samoan plume and the Tonga–Kermadec slabs, *Nat. Commun.,* **7**(1), 1–9.

Dahlen, F. & Tromp, J., 1998. *Theoretical Global Seismology,* Princeton Univ. Press.

Deuss, A., Ritsema, J. & van Heijst, H.-J., 2013. A new catalogue of normal-mode splitting function measurements up to 10 mHz, *Geophys. J. Int.,* **192**(3), 920–937.

Dziewonski, A. & Anderson, D., 1981. Preliminary reference Earth model, *Phys. Earth planet. Inter.,* **25**(4), 297–356.

Edmonds, A., 1960. *Angular Momentum in Quantum Mechanics,* Princeton Univ. Press.

Ferreira, A., Woodhouse, J., Visser, K. & Trampert, J., 2010. On the robustness of global radially anisotropic surface wave tomography, *J. geophys. Res.,* **115**(B4), doi:10.1029/2009JB006716.

French, S. & Romanowicz, B., 2014. Whole-mantle radially anisotropic shear velocity structure from spectral-element waveform tomography, *Geophys. J. Int.,* **199**(3), 1303–1327.

Gu, Y.J., Lerner-Lam, A.L., Dziewonski, A.M. & Ekström, G., 2005. Deep structure and seismic anisotropy beneath the east Pacific rise, *Earth planet. Sci. Lett.,* **232**(3–4), 259–272.

Kemper, J., van Driel, M., Munch, F., Khan, A. & Giardini, D., 2022. A spectral element approach to computing normal modes, *J. geophys. Int.,* **229**(2), 915–932.

Kendall, J.-M. & Silver, P.G., 1996. Constraints from seismic anisotropy on the nature of the lowermost mantle, *Nature,* **381**(6581), 409–412.

Koelemeijer, P., Deuss, A. & Trampert, J., 2012. Normal mode sensitivity to Earth's D″ layer and topography on the core–mantle boundary: what we can and cannot see, *Geophys. J. Int.,* **190,** 553–568.

Koelemeijer, P., Deuss, A. & Ritsema, J., 2013. Observations of core-mantle boundary Stoneley modes, *Geophys. Res. Lett.,* **40**(11), 2557–2561.

Koelemeijer, P., Ritsema, J., Deuss, A. & Van Heijst, H.-J., 2016. SP12RTS: a degree-12 model of shear-and compressional-wave velocity for Earth's mantle, *Geophys. J. Int.,* **204**(2), 1024–1039.

Koelemeijer, P.J., 2014. Normal mode studies of long wavelength structures in Earth's lowermost mantle, *PhD thesis*, University of Cambridge, Cambridge, UK.

Kustowski, B., Ekström, G. & Dziewoński, A., 2008. Anisotropic shear-wave velocity structure of the Earth's mantle: a global model, *J. geophys. Res.,* **113**(B6), doi:10.1029/2007JB005169.

Laske, G., Masters, G., Ma, Z. & Pasyanos, M., 2013. Update on crust1. 0—a 1-degree global model of Earth's crust, in *Proceedings of the EGU General Assembly 2013, Geophys. res. abstr.,* held 7-12 April, 2013 in Vienna, Austria, id. EGU2013-2658.

Lay, T. & Helmberger, D.V., 1983. The shear-wave velocity gradient at the base of the mantle, *J. geophys. Res.,* **88**(B10), 8160–8170.

Long, M.D. & Becker, T.W., 2010. Mantle dynamics and seismic anisotropy, *Earth planet. Sci. Lett.,* **297**(3–4), 341–354.

Love, A.E.H., 1927. *A Treatise on the Mathematical Theory of Elasticity,* Cambridge Univ. Press.

Mainprice, D., 2010. Seismic anisotropy of the deep earth from a mineral and rock physics perspective, in *Treatise on Geophysics,* 2nd edn, Vol. 2: Mineral Physics, pp. 487–538, Elsevier.

Marone, F. & Romanowicz, B., 2007. Non-linear crustal corrections in high-resolution regional waveform seismic tomography, *J. geophys. Int.,* **170**(1), 460–467.

Masters, G., Laske, G. & Gilbert, F., 2000. Matrix autoregressive analysis of free-oscillation coupling and splitting, *Geophys. J. Int.,* **143**(2), 478–489.

Meade, C., Silver, P.G. & Kaneshima, S., 1995. Laboratory and seismological observations of lower mantle isotropy, *Geophys. Res. Lett.,* **22**(10), 1293–1296.

Meier, U., Curtis, A. & Trampert, J., 2007. Global crustal thickness from neural network inversion of surface wave data, *J. geophys. Int.,* **169**(2), 706–722.

Montagner, J.-P., 2002. Upper mantle low anisotropy channels below the pacific plate, *Earth planet. Sci. Lett.,* **202**(2), 263–274.

Montagner, J.-P. & Nataf, H.-C., 1986. A simple method for inverting the azimuthal anisotropy of surface waves, *J. geophys. Res.,* **91**(B1), 511–520.

Montagner, J.-P. & Tanimoto, T., 1991. Global upper mantle tomography of seismic velocities and anisotropies, *J. geophys. Res.,* **96**(B12), 20 337–20 351.

Mooney, W., Laske, G. & Masters, T., 1998. CRUST 5.1: a global crustal model at 5× 5 °, *J. geophys. Res.,* **103**(B1), 727–747.

Moulik, P. & Ekström, G., 2014. An anisotropic shear velocity model of the Earth's mantle using normal modes, body waves, surface waves and long-period waveforms, *Geophys. J. Int.,* **199**(3), 1713–1738.

Moulik, P. & Ekström, G., 2016. The relationships between large-scale variations in shear velocity, density, and compressional velocity in the Earth's mantle, *J. geophys. Res.,* **121**(4), 2737–2771.

Nataf, H.-C. & Ricard, Y., 1996. 3smac: an a priori tomographic model of the upper mantle based on geophysical modeling, *Phys. Earth planet. Inter.,* **95**(1–2), 101–122.

Nowacki, A. & Cottaar, S., 2021. Toward imaging flow at the base of the mantle with seismic, mineral physics, and geodynamic constraints, in *Mantle Convection and Surface Expressions,* Chapter 13, Geophysical Monograph Series, pp. 329–352, eds Marquardt, Hauke, Ballmer, Maxim, Cottaar, Sanne & Konter, Jasper, AGU.

Nowacki, A., Wookey, J. & Kendall, J.-M., 2011. New advances in using seismic anisotropy, mineral physics and geodynamics to understand deformation in the lowermost mantle, *J. Geodyn.,* **52**(3–4), 205–228.

Panning, M. & Romanowicz, B., 2006. A three-dimensional radially anisotropic model of shear velocity in the whole mantle, *Geophys. J. Int.,* **167**(1), 361–379.

Panning, M., Lekić, V. & Romanowicz, B., 2010. Importance of crustal corrections in the development of a new global model of radial anisotropy, *J. geophys. Res.,* **115**(B12), doi:10.1029/2010JB007520.

Resovsky, J.S. & Ritzwoller, M.H., 1998. New and refined constraints on three-dimensional Earth structure from normal modes below 3 mHz, *J. geophys. Res.,* **103**(B1), 783–810.

Restelli, F., Koelemeijer, P. & Ferreira, A.M., 2022. Normal mode splitting function predictions for mantle anisotropy (version v2) [data set], doi:10.5281/zenodo.7101457.

Ritsema, J., Van Heijst, H., Woodhouse, J. & Deuss, A., 2009. Long-period body wave traveltimes through the crust: implication for crustal corrections and seismic tomography, *J. geophys. Int.,* **179**(2), 1255–1261.

Ritsema, J., Deuss, A., van Heijst, H.-J. & Woodhouse, J.H., 2011. S40RTS: a degree-40 shear-velocity model for the mantle from new Rayleigh wave dispersion, teleseismic traveltime and normal-mode splitting function measurements, *Geophys. J. Int.,* **184**(3), 1223–1236.

Romanowicz, B. & Wenk, H.-R., 2017. Anisotropy in the deep earth, *Phys. Earth planet. Inter.,* **269,** 58–90.

Schaefer, J., Boschi, L., Becker, T. & Kissling, E., 2011. Radial anisotropy in the European mantle: tomographic studies explored in terms of mantle flow, *Geophys. Res. Lett.,* **38**(23), doi:10.1029/2011GL049687.

Schneider, S. & Deuss, A., 2021. A new catalogue of toroidal-mode overtone splitting function measurements, *J. geophys. Int.,* **225**(1), 329–341.

Shephard, G.E., Matthews, K.J., Hosseini, K. & Domeier, M., 2017. On the consistency of seismically imaged lower mantle slabs, *Sci. Rep.,* **7**(1), doi:10.1038/s41598-017-11039-w.

Soldati, G., Koelemeijer, P., Boschi, L. & Deuss, A., 2013. Constraints on core-mantle boundary topography from normal mode splitting, *Geophys. Geochem. Geosys.,* **14**(5), 1333–1342.

Tarantola, A., 1987. *Inverse Problem Theory,* Elsevier.

Tesoniero, A., Auer, L., Boschi, L. & Cammarano, F., 2015. Hydration of marginal basins and compositional variations within the continental lithospheric mantle inferred from a new global model of shear and compressional velocity, *J. geophys. Res.,* **120**(11), 7789–7813.

Walpole, J., Wookey, J., Kendall, J.-M. & Masters, T.-G., 2017. Seismic anisotropy and mantle flow below subducting slabs, *Earth planet. Sci. Lett.,* **465,** 155–167.

Wang, N., Montagner, J.-P., Fichtner, A. & Capdeville, Y., 2013. Intrinsic versus extrinsic seismic anisotropy: the radial anisotropy in reference earth models, *Geophys. Res. Lett.,* **40**(16), 4284–4288.

Wessel, P., Smith, W. H.F., Scharroo, R., Luis, J. & Wobbe, F., 2013. Generic mapping tools: Improved version released, *EOS, Trans. Am. geophys. Un.,* **94**(45), 409–410.

Woodhouse, J., Giardini, D. & Li, X., 1986. Evidence for inner core anisotropy from free oscillations, *Geophys. Res. Lett.,* **13**(13), 1549–1552.

Zaroli, C., 2016. Global seismic tomography using Backus–Gilbert inversion, *Geophys. Suppl. Mon. Not. R. Astron. Soc.,* **207**(2), 876–888.

SUPPORTING INFORMATION

Supplementary data are available at *GJI* online.

Figure S1. Example sensitivity kernels of spheroidal and toroidal modes for structure at $s = 0$ (red), $s = 2$ (blue) and $s = 4$ (black). Similar to Fig. 2 in the main text.

Figure S2. Histograms of degree 2 observability values for different v_s anisotropy patterns (O_2^{pattern}), computed using the normalized anisotropic models indicated at the top, with SGLOBE-rani as reference model. Similar to Fig. 7 in the main text, but now anisotropy is only included in the depth range 25–220 km.

Figure S3. Effect of different structures in the mantle on the frequencies of spheroidal modes. Similar to Fig. 10 in the main text, but now showing coefficients for degree 4, including results for real ($\Re$) and imaginary ($\Im$) coefficients. Deviations in frequency are shown relative to predictions for isotropic SEMUCB-WM1 with CRUST-SEM and a constant v_p scaling factor ($d\ln v_p = 0.5 \times d\ln v_s$). We compare the effect of (a) including anisotropy, (b) changing the crustal thickness model to CRUST2.0 and (c) changing the v_p scaling to be depth dependent (as described in the main text). See the caption of Fig. 10 for more details.

Figure S4. Effect of different structures in the mantle on the frequencies of spheroidal modes. Similar to Fig. 10 in the main text and Fig. S3, but now showing deviations from isotropic model SGLOBE-rani with CRUST-SG and a constant v_p scaling factor ($d\ln v_p = 0.5 \times d\ln v_s$). We compare the effect of (a) including vs anisotropy, (b) changing the crustal thickness model to CRUST2.0 and (c) changing the v_p scaling to be depth-dependent (as described in the main text). See the caption of Fig. 10 for more details.

Figure S5. Plot representing the degree 2 integrated sensitivity of (a–d) spheroidal modes and (e–f) toroidal modes to (a,e) v_{sh}, (b,f) v_{sv}, (c) v_{ph} and (d) v_{pv}. Each square represents a normal mode of radial and angular order n and l, and the colour of each square indicates the depth-integrated sensitivity of each mode to the indicated parameter. Hence, light colours indicate low overall sensitivity, dark colours high sensitivity.

Figure S6. Observed and predicted splitting function maps for mode ${}_0S_{26}$ plotted up to spherical harmonic degree 10. (a) Observed splitting function from Koelemeijer *et al*. (2013). Panels (b) and (c) show predicted splitting functions for different crustal models and different anisotropy models respectively. Specifically, we show in (a) predictions for isotropic SEMUCB-WM1 with different crustal thickness models; CRUST-SEM (top), CRUSTSG (middle) and CRUST2.0 (bottom). In (b) we compare predictions for anisotropic models SEMUCB-WM1 (top), SGLOBE-rani (middle) and S362WMANI+M (bottom), respectively with CRUST-SEM, CRUST-SG and CRUST2.0 on top.

Figure S7. Observed and predicted splitting function maps for mode ${}_2T_7$ plotted up to degree 6. (a) Observed splitting function from Schneider and Deuss (2021). Panels (b) and (c) show predicted splitting functions for different crustal models and different anisotropy models, respectively. See the caption of Fig. S6 for more details.

Table S1. List of spheroidal and toroidal modes used in this study, including the references from which splitting function coefficients are taken [MLG00 = Masters *et al*. (2000), DRvH13 = Deuss *et al*. (2013), KDR13 = Koelemeijer *et al*. (2013), K14 = Koelemeijer (2014), RR98 = Resovsky & Ritzwoller (1998) and SD21 = Schneider & Deuss (2021)].

Table S2. Misfit to toroidal mode observations for prediction using models SAW642ANb, savani, SEMUCBWM1, S362WMANI+M, SGLOBE-rani and SPani. In the different columns, we compare the misfit results for all modes for isotropic predictions (Iso - All) and anisotropic predictions (Aniso - All). In each case, we show the misfit for degree 2 ($s = 2$) only or all degrees together ($s =$ all, up to $s = 6$). Bold values indicate the lowest misfit in each column.